Spin-State Control and Ferromagnetism in $LaCoO_3$ through Non-Magnetic-Ion Substitution Effects
(非磁性イオン置換効果を通して起こる $LaCoO_3$ におけるスピン状態制御と強磁性)

浅井　晋一郎

Contents

Chapter 1

Introduction

1.1 Background

All materials surrounding us consist of only one hundred species of the elements, and their various properties are dependent on the state of their electrons. Valence electrons are most important for determining the properties of the materials. When the Coulomb repulsion between the electrons is large enough compared with the energy gain of the kinetic energy due to the transfer integral, the electrons are localized even in the partially occupied electron orbitals. These electrons prefer to occupy the different orbitals with each other owing to the intra-atomic Coulomb repulsion (the Hund coupling). Furthermore, the electrons in the material have the influence from the inter-atomic Coulomb repulsion, which can be treated as crystal field in a simple approximation.

Let us discuss the case of the electrons in fivefold degenerate d orbitals sur-

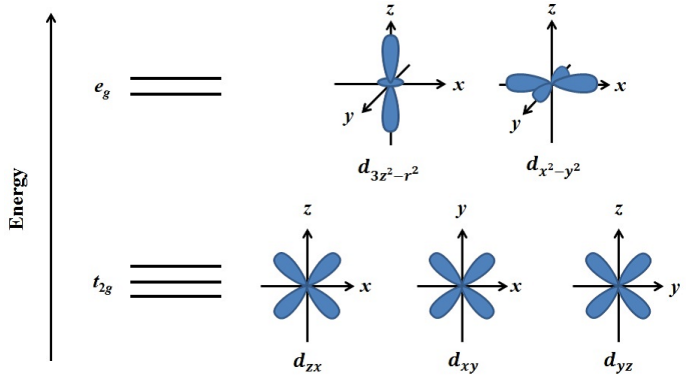

Figure 1.1: Energy levels of the d orbitals in the cubic crystal field. Schematic pictures of the $d_{3z^2-r^2}$, $d_{x^2-y^2}$, d_{xy}, d_{yz}, and d_{zx} orbitals are shown in the right side.

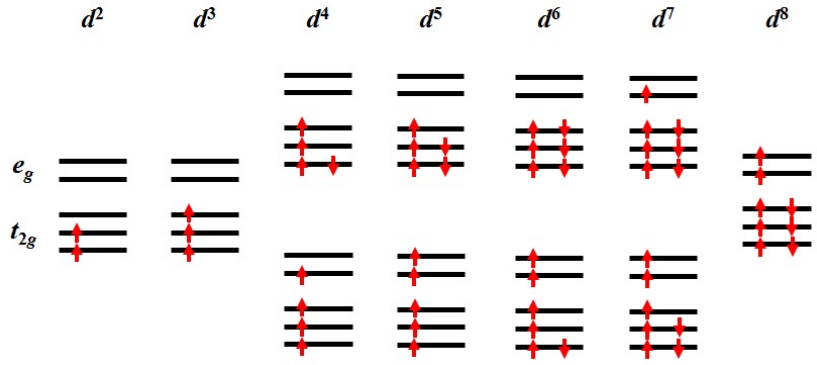

Figure 1.2: Ground states of d^n electrons in cubic crystal field for $2 \leq n \leq 8$. Low-spin states and high-spin states are shown in the upper and lower side for $4 \leq n \leq 7$, respectively.

rounded by eight point charges octahedrally, which is seen in the perovskite-type compounds. In this case, the d orbitals are split into the doubly degenerate e_g orbitals and the triply degenerate t_{2g} orbitals as shown in Fig. 1.1, which is called crystal field splitting. The e_g orbitals composed of $d_{3z^2-r^2}$ and $d_{x^2-y^2}$ locate in upper energy levels than t_{2g} orbitals composed of d_{xy}, d_{yz}, and d_{zx} owing to the Coulomb repulsion. The configuration of the electrons in the d orbitals (spin state) and their relative energy were investigated in detail by Tanabe and Sugano [1,2]. Figure 1.2 shows the ground state of d^n electrons in the cubic crystal field for $2 \leq n \leq 8$. The systems of d^n electrons for $4 \leq n \leq 7$ can take two different states as the ground state depending on the strength of the crystal field. Which state is more stable is determined by the interplay between the Hund coupling energy and the Coulomb repulsion with the ligand charges. When the Hund coupling energy is larger than the Coulomb repulsion, the electrons prefer to occupy the different orbitals with no regard to the energy gap between e_g and t_{2g} orbitals, as shown in the lower side in Fig. 1.2. For the opposite condition, the electrons preferentially occupy the t_{2g} orbitals, as shown in the upper side in Fig. 1.2. These spin states are called high-spin state (HS) and low-spin state (LS). When the Hund coupling energy competes with the crystal field splitting, the spin state can be changed with temperature variation, magnetic field, light irradiation, or pressure, known as spin crossover (spin-state crossover).

Thermally induced spin-state crossover is a crossover of the stable state from the LS state to the HS state with increasing temperature owing to the entropy gain. When the spin-state crossover occurs, all the ions change from the LS state to the HS state with increasing temperature because the HS state is energetically stable at high temperature. It is different from the thermal excitation in which the ions are in thermal equilibrium with the excited HS state

at high temperature. The first spin-state crossover complex for the d^6 system $Fe(phen)_2X_2$ (phen = 1,10-phenanthroline; X = SCN, SeCN) were synthesized in 1964 [3], and the spin-state crossover from the LS state (t_{2g}^6) to HS state ($e_g^2 t_{2g}^4$) was identified in 1967 [4]. In a crystal, cooperative phenomena can affect the spin-state crossover. For $Fe(phen)_2(NCS)_2$, the transition entropy evaluated from the specific heat is much larger than that expected from the magnetic entropy change, which suggests that the phonon contribution should be taken into account [5]. Many Fe(II) complexes have been extensively investigated because of its attracting nature due to the reversible switching between the non-magnetic and magnetic states.

Perovskite type oxide $LaCoO_3$ has been extensively investigated as a spin-state crossover compound since Heikes *et al.* reported anomalous magnetic properties [6]. The spin state of Co^{3+} ions in $LaCoO_3$ can be controlled with temperature variation [7], magnetic field [8], or pressure [9]. The magnetization of $LaCoO_3$ rapidly increases with increasing temperature up to 90 K owing to spin-state crossover of $Co^{3+}(3d^6)$ ions. The other properties also suggest the spin-state crossover of Co^{3+} ions, which is reviewed in the section 1.2. The magnetization shows a Curie-Weiss-like behavior at room temperature, indicating that the spin-state crossover is almost finished. However, the magnetization is much smaller than that expected from the HS Co^{3+} ions, which implies that the spin state of Co^{3+} ions cannot be described as the HS state at room temperature. The spin state of Co^{3+} ions at room temperature has been under debate until now, which is briefly summarized in the section 1.3.

In contrast to $LaCoO_3$, $LaRhO_3$ is non-magnetic material [10] because Rh^{3+} ions ($4d^6$) prefer to take the LS state owing to its wide $4d$ orbitals inducing the large crystal field splitting. In 2003, Kyômen *et al.* have investigated the magnetization of $LaCo_{1-x}M_xO_3$ (M=Rh, Ga, Al) and found that the Rh substitution induces the magnetization at low temperature [11]. Because the two mother compound $LaCoO_3$ and $LaRhO_3$ are non-magnetic at low temperature, the magnetization cannot be explained by a conventional way. We explain the previous study for the non-magnetic-ion substitution effects on $LaCoO_3$ in the section 1.4.

In this thesis, we control and discuss the spin state of Co^{3+} ions in $LaCoO_3$ through the non-magnetic-ion substitution effects. For this purpose, we first investigate the structural and magnetic properties of $LaCo_{1-x}Rh_xO_3$, which is shown in Chapters 2 and 3, respectively. The investigation of the structural and magnetic properties are complementary. From the structural analysis based on the diffraction measurements, we can see the change of the lattice volume due to the spin-state crossover. On the other hand, the change of lattice volume due to the spin-state crossover is a few percents of the volume, which makes it difficult to discuss the non-magnetic-ion substitution effects quantitatively. The analysis of the magnetization is more suitable for

the quantitative discussion because all the elements except for the magnetic Co^{3+} ions are non-magnetic in this system. On one hand, the analysis of the magnetization is difficult for the spin-state crossover compound because the temperature-dependent number of the magnetic Co^{3+} ions induces the complicated temperature dependence of the magnetization. The information obtained from the structural properties is thus needed in order to discuss the magnetic properties. For quantitative analysis of the lattice volume and magnetization, we regard the different spin states of Co^{3+} ions as the different species of ions having their unique ionic radii and magnetic moment, and assume a homogeneous solid solution of Co^{3+}, Rh^{3+}, and Ga^{3+} ions in the Rh and/or Ga substituted samples. We can evaluate the HS Co^{3+} content from the lattice volume and the magnetization, which are consistent with each other. We have found from the neutron diffraction measurements that the CoO_6 octahedra are almost regular, indicating that the HS Co^{3+} ions are reasonable for the magnetic ions. In the investigation of the magnetic properties, we have found the ferromagnetic ordering of $LaCo_{1-x}Rh_xO_3$ for $0.1 \leq x \leq 0.4$. We discuss the nature of the ordering through the magnetization and neutron scattering measurements. In order to discuss the Rh substitution effects in detail, we investigate the Ga substitution effects on the spin state of Co^{3+} ions and compare them with the Rh substitution effects in Chapter 4. We conclude that the difference between the non-magnetic-ion substitution effects cannot be explained if all the Co^{3+} ions have the identical spin state, which supports that there are HS Co^{3+} and LS Co^{3+} ions in $LaCoO_3$ at room temperature. Finally, we give a brief summary in Chapter 5.

1.2 Perovskite type oxide $LaCoO_3$

1.2.1 Structural property

In this section, we introduce the physical properties of $LaCoO_3$ related with the spin-state crossover. The cobalt oxide $LaCoO_3$ has the distorted perovskite structure with a space group $R\bar{3}c$ as shown in Fig. 1.3(a) and 1.3(b). The lattice parameters a and angle α are estimated to be 5.38 and 60.8° at room temperature, respectively [12]. The CoO_6 octahedra are little distorted with remaining the isotropic Co-O bond length. Figure1.4 shows the temperature dependence of the lattice volume for $LaCoO_3$ and $La_{0.92}Sr_{0.08}CoO_3$. For $La_{0.92}Sr_{0.08}CoO_3$, the temperature dependence of the lattice volume is well fitted by Grüneisen-Einstein formula. Grüneisen-Einstein formula is derived from the free energy of the lattice. The free energy of the lattice related with the lattice expansion can be written by the sum of the elastic strain energy and the free energy of the phonon, which is given by

$$F(\Delta, T) = \frac{1}{2}B\Delta^2 + \sum_i k_{\mathrm{B}}T \ln[2\sinh(\frac{\hbar\omega_i}{k_{\mathrm{B}}T})], \tag{1.1}$$

where Δ, B, and ω represent the difference of the lattice volume from that at 0 K, the bulk modulus, and the frequency of the phonon, respectively. The lattice volume is related with the frequency of the phonon owing to the

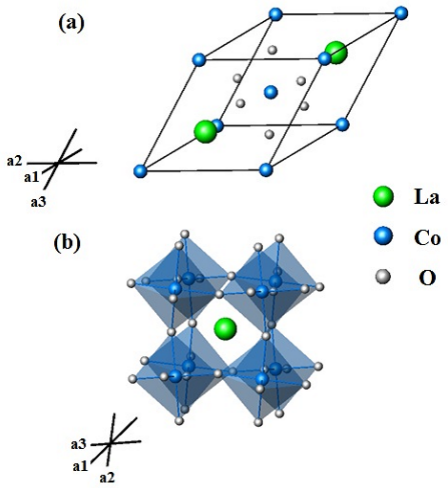

Figure 1.3: (a) Crystal structure of $LaCoO_3$. The solid lines shows the rhombohedral unit cell. For better understanding, we shows the eight adjacent CoO_6 octahedra with one La atom in $LaCoO_3$, as shown in Fig. (b).

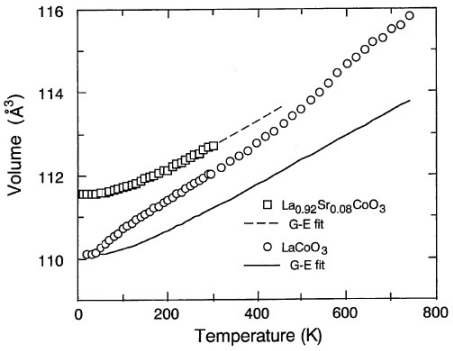

Figure 1.4: Temperature dependence of the lattice volume for two chemical formulas of $LaCoO_3$ and $La_{0.92}Sr_{0.08}CoO_3$ [12]. The dotted and solid lines are based on Grüneisen-Einstein model (see text).

anharmonic terms of the interatomic potential, which is expressed by

$$\gamma_i = -\frac{\partial \ln \omega_i}{\partial \ln V}, \tag{1.2}$$

where γ is defined as Grüneisen parameter. By using the equation 1.1 and 1.2, we can derive the lattice volume as a function of temperature (Grüneisen-Einstein formula) when the Einstein model is used for the phonon distribution,

$$V_{\mathrm{GE}}(T) = V(0\ \mathrm{K})\{1 + \frac{\alpha_{\mathrm{V}}\, T_{\mathrm{E}}}{2}(\coth(\frac{T_{\mathrm{E}}}{2\,T}) - 1)\}, \tag{1.3}$$

where T_{E} and α_{V} represent the Einstein temperature and the thermal expansion coefficient for $T \gg T_{\mathrm{E}}$ as expressed

$$T_{\mathrm{E}} = \frac{\hbar\omega}{k_{\mathrm{B}}} \tag{1.4}$$

and

$$\alpha_{\mathrm{V}} = \frac{\gamma k_{\mathrm{B}}}{BV(0\ \mathrm{K})}, \tag{1.5}$$

respectively.

In contrast, the lattice volume of $LaCoO_3$ anomalously increases with increasing temperature from 50 K owing to the spin-state crossover. We should note that the thermal expansion coefficient of $LaCoO_3$ is much larger than that of other perovskite oxides even at room temperature [13], which indicates the spin-state crossover is not completely finished. The change of the detail crystal structure with temperature from 5 to 1000 K was investigated by the powder neutron scattering [14], which shows that the additional lattice expansion of $LaCoO_3$ is due to the change of the Co-O bond length with temperature. The spin-state crossover of Co^{3+} ions affects the dynamic and

local distortion of the crystal structure. Pair density function (PDF) analysis of neutron diffraction for $LaCoO_3$ [15] at 20 K can be explained by the crystal structure with the space group $R\bar{3}c$. The additional peaks in PDF appear with increasing temperature, and the PDF at 300 K deviate from that expected from the average crystal structure determined by the diffraction measurements. The infrared spectroscopy [16] and Raman scattering [17] suggest that the additional phonon modes grows with increasing temperature. These experimental results suggest that the local crystal structure is modified by the spin-state crossover with remaining the $R\bar{3}c$ average crystal structure. The small thermal conductivity above 100 K also suggests the lattice disordering effects [18].

1.2.2 Magnetic property

Figure 1.5(a) shows the temperature dependence of the magnetic susceptibility and reciprocal susceptibility for $LaCoO_3$ [12]. The magnetization is non-magnetic at the lowest temperature, except for the upturn at the lowest temperature owing to the lattice defects [19]. The anomalous increase of the magnetization around 100 K thus indicates that the spin state of Co^{3+} ions

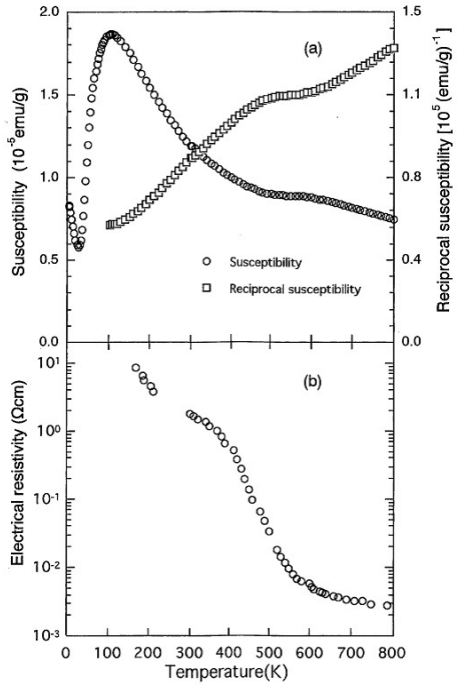

Figure 1.5: (a) Temperature dependence of the magnetic susceptibility and reciprocal susceptibility for $LaCoO_3$. (b) Electrical resistivity of $LaCoO_3$ as a function of temperature [12].

are changed from non-magnetic to magnetic one, which is also suggested by the experimental results of ESR [20] and NMR [21]. From 150 to 350 K, the magnetic susceptibility decreases with increasing temperature, and its reciprocal can be fitted by the linear function. This behavior is often seen for the paramagnetic materials known as Curie-Weiss law. Curie-Weiss law is derived as the expected value for the magnetization of the system in which there are spins having the number N and the quantum number S under the magnetic field $\mu_0 H$ at the temperature T. When we introduce the nearest neighbor magnetic interaction J between spins, the energy of the spin in the i site E_i having the magnetic quantum number S_i ($\mathrm{S}_i = \mathrm{S}, \mathrm{S}-1, ..., -\mathrm{S}$) is derived,

$$E_i = -g\mu_0\mu_\mathrm{B}\mathrm{S}_i H - \sum_j J\mathrm{S}_i\mathrm{S}_j. \tag{1.6}$$

g and μ_B are g factor and Bohr magnetron, respectively. We take the sum of j for all the nearest neighbor cites. For simplicity, we approximate the second terms to the mean internal magnetic field as expressed,

$$\sum_j J\mathrm{S}_i\mathrm{S}_j = zJ\mathrm{S}_i\langle\mathrm{S}_j\rangle = zJ\langle\mathrm{S}_i\rangle\mathrm{S}_i. \tag{1.7}$$

z is the number of the nearest neighbor cites. The expected value for the magnetization is thus derived as,

$$M = Ng\mu_\mathrm{B}\langle\mathrm{S}_i\rangle = \frac{Ng\mu_\mathrm{B}\sum_{\mathrm{S}_i=-\mathrm{S}}^{\mathrm{S}}\mathrm{S}_i\exp\left(-E_i/k_\mathrm{B}T\right)}{\sum_{\mathrm{S}_i=-\mathrm{S}}^{\mathrm{S}}\exp\left(-E_i/k_\mathrm{B}T\right)}, \tag{1.8}$$

and

$$E_i = -g\mu_0\mu_\mathrm{B}\mathrm{S}_i H - zJ\langle\mathrm{S}_i\rangle\mathrm{S}_i = -g\mu_0\mu_\mathrm{B}\mathrm{S}_i H - \frac{zJM}{Ng\mu_\mathrm{B}}\mathrm{S}_i. \tag{1.9}$$

Instead of solving the self-consistent equation (1.8), we consider the paramagnetic state where $|E_i| \ll k_\mathrm{B}T$. Then, Eq. (1.8) is approximated to

$$M = \frac{N\mu_0\mu_B^2\mu_\mathrm{eff}^2 H}{3k_\mathrm{B}T} + M\frac{zJ\mathrm{S}(\mathrm{S}+1)}{3k_\mathrm{B}T}, \tag{1.10}$$

where the effective magnetic moment μ_eff is defined as

$$\mu_\mathrm{eff} = g\sqrt{\mathrm{S}(\mathrm{S}+1)}. \tag{1.11}$$

Let us define the Weiss temperature θ as

$$\theta = -\frac{zJ\mathrm{S}(\mathrm{S}+1)}{3k_\mathrm{B}}. \tag{1.12}$$

Thus, we obtain the Curie-Weiss law,

$$\frac{M}{\mu_0 H} = \frac{N\mu_\mathrm{B}^2\mu_\mathrm{eff}^2}{3k_\mathrm{B}(T+\theta)}, \tag{1.13}$$

where the $\mu_{\rm eff}$ and θ have the information about the spins and their interaction, respectively. $\mu_{\rm eff}$ of $LaCoO_3$ evaluated from the magnetic susceptibility for 150 and 350 K are 3.4 $\mu_{\rm B}$, which is much smaller than that expected from the HS Co^{3+} ions (4.9 $\mu_{\rm B}$) [22]. It indicates that the spin state of Co^{3+} ions in $LaCoO_3$ is not HS state at room temperature. There are many experimental and theoretical discussion about the spin state of Co^{3+} ions, which is shown in the section 1.3. We can see the plateau in the magnetic susceptibility around 500 K, where the electrical resistivity significantly drops with increasing temperature as shown in 1.5(b). The optical conductivity shows the charge gap of 0.1 eV closes at around 500 K, which means the insulator-metal transition takes place [23]. $\mu_{\rm eff}$ of 4.1 $\mu_{\rm B}$ is evaluated from the magnetic susceptibility above 650 K [22]. The large localized moment evaluated from the susceptibility is inconsistent with the low electrical resistivity indicating the many conductive electrons. There are many discussion on the spin state of Co^{3+} ions above 650 K, which is unclear until now. The Weiss temperatures are evaluated to be 185 and 504 K from the magnetization for 150 and 350 K and above 650 K, respectively [22]. It indicates that the interaction between the magnetic Co^{3+} ions is antiferromagnetic, which is probable for the magnetic interaction between the magnetic ions in the perovskite oxides. On the other hand, the polarized neutron measurements indicate the weak ferromagnetic interaction between the magnetic Co^{3+} ions [24]. The ferromagnetic ordering emerges by suppressing spin-state crossover in the nanoparticles [25], nanoribbons [26], and biaxially strained thin film [27] of $LaCoO_3$. The magnetic interaction between the Co^{3+} ions in this oxide should be discussed in relation to the spin state of Co^{3+} ions.

1.3 Spin state of Co^{3+} ions for $LaCoO_3$ at room temperature

1.3.1 HS-LS model

In this section, we introduce the discussion on the spin state of Co^{3+} ions in $LaCoO_3$ emerging from 100 to 350 K. As shown above, $\mu_{\rm eff}$ of $LaCoO_3$ evaluated from the magnetic susceptibility is 3.4 $\mu_{\rm B}$, which is much smaller than that expected from the HS Co^{3+} ions (4.9 $\mu_{\rm B}$). Here, we show two models which can explain the small magnetization. The one model is that there are HS and LS Co^{3+} ions in $LaCoO_3$ at room temperature (HS-LS model). Raccah and Goodenough proposed that the displacements of O^{2-} ions toward $Co_{\rm I}$ sites as shown in Fig. 1.6 makes two different crystal fields, which stabilizes the LS and HS Co^{3+} ions in $Co_{\rm I}$ and $Co_{\rm II}$ sites, respectively [28]. The first-principle calculation suggests that the HS-LS ordered state is probable for the spin state of Co^{3+} ions [29]. However, the NaCl-type spin-state ordering is not probable in the crystal structure of $LaCoO_3$ in which the Co ions are equiva-

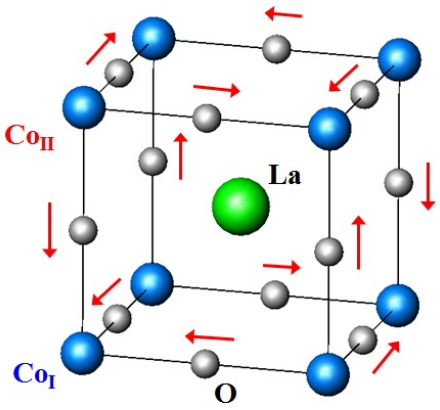

Figure 1.6: Proposed displacements of the O^{2-} ions in the perovskite $LaCoO_3$. The arrows represent the direction of the displacements. For simplicity, the cubic perovskite structure is shown.

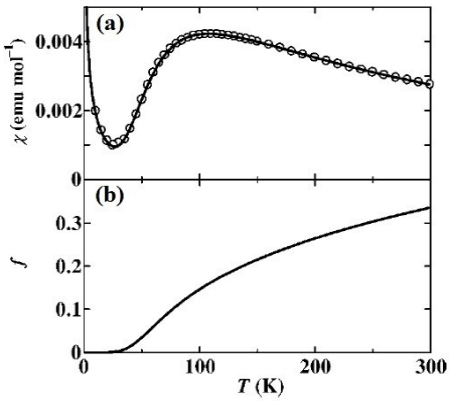

Figure 1.7: (a) Temperature dependence of the magnetic susceptibility for $LaCoO_3$. The open circles and solid line shows the experimental data and fitting curves, respectively [32]. (b) Fraction of Co ions in the HS state evaluated from the fitting [32].

lent. No experimental evidence for such a spin-state order has been observed until now. On the other hand, many experimental and theoretical results suggest that the HS Co^{3+} ions are probable as the magnetic ions in $LaCoO_3$. The anisotropic g factor $g_{\parallel}$, $g_{\perp}$, and the effective spin S for the spin state of magnetic Co^{3+} ions is evaluated to be 3.35, 3.55, and 1 from ESR spectra, respectively [20], which indicates that the orbital angular momentum is not quenched by the crystal field splitting. The calculation taking the spin-orbit interaction into account suggests that the spin state of magnetic Co^{3+} ions is HS state with the orbital momentum $L = 1$ [30], which is consistent with

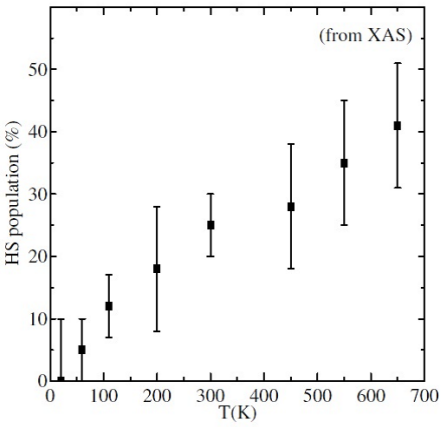

Figure 1.8: HS Co^{3+} content evaluated from fitting the XAS spectra as a function of temperature [31].

the magnetic circular dichroism measurements [31]. The magnetic susceptibility are reproduced by the calculation using the proposed energy diagram as shown in Fig. 1.7(a), when the energy gap between the HS and LS state is dependent on the HS Co^{3+} content and there is the energy gain owing to mixing the two spin state [32]. The temperature dependence of the HS Co^{3+} content evaluated from the magnetization is shown in Fig. 1.7(b). The HS Co^{3+} content of 0.3 per formula units (f. u.) gradually decreases down to 0 with decreasing temperature owing to the temperature-dependent energy gap. The HS Co^{3+} content evaluated from fitting the XAS spectra as a function of temperature is shown in Fig. 1.8 [31], which is quantitatively consistent with that evaluated from the magnetic susceptibility. These experimental results suggest that the content of the HS Co^{3+} ions is about 0.3 per f. u. at room temperature.

1.3.2 IS model

The other model is that the spin state of Co^{3+} ions is interpreted as the intermediate-spin state (IS;$e_g^1 t_{2g}^5$). We should emphasize that the IS state cannot be stable in Tanabe-Sugano diagram [2]. Potze *et al.* theoretically suggested that the Co^{3+} ions can take IS state owing to the hybridization between the e_g orbitals and O $2p$ orbitals [33]. The calculations using the local-density approximation (LDA+U) suggest that the IS state is reasonable for the spin state of Co^{3+} ions in $LaCoO_3$ at room temperature [34]. The existence of IS Co^{3+} ions has been long discussed not only in $LaCoO_3$ but also in other Co compounds. The metallic state in $La_{1-x}Sr_xCoO_3$ with ferromagnetic ordering is interpreted as the mixture of the LS Co^{4+} and IS Co^{3+} ions [35]. Recently, the IS Co^{3+} ions with the orbital ordering are experimen-

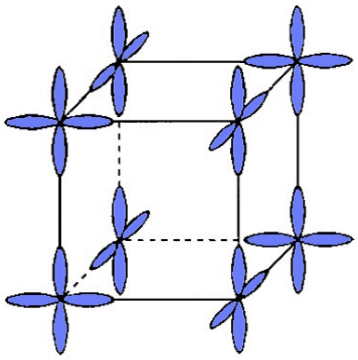

Figure 1.9: Orbital ordering of IS Co^{3+} proposed by Korotin *et al.* [34]

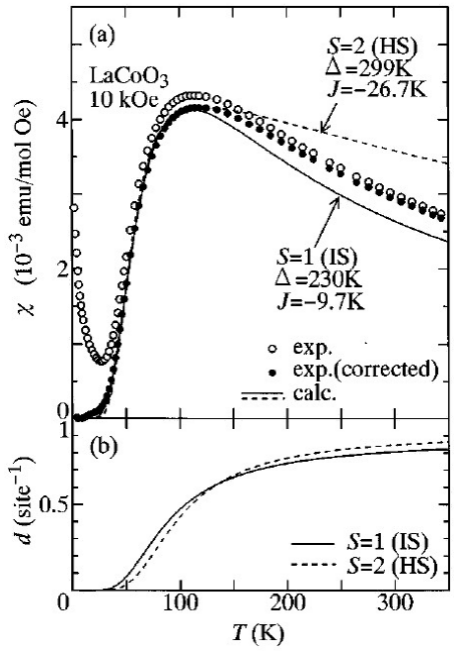

Figure 1.10: (a) Temperature dependence of the magnetic susceptibility for $LaCoO_3$ [16]. The open and solid circles represents the experimental data and the corrected one by subtracting the Curie-Weiss-like contribution at the lowest temperature. The solid and broken lines shows the fitting curves. The parameters S, J, and Δ represents the quantum spin number of the magnetic Co^{3+} ion, the magnetic interaction, and the energy gap between the LS and the magnetic state of Co^{3+} ions, respectively. (b) Fraction of Co ions in the IS state evaluated from the fitting [16].

tally identified in $Sr_3YCo_4O_{10.5}$ [36]. For $LaCoO_3$, the orbital ordering with

the Jahn-Teller distortion as shown in Fig. 1.9 is proposed for IS model in order to explain the semiconductive electrical transport at room temperature [34]. The structural analysis by using the synchrotron x-ray diffraction suggests the distortion of CoO_6 octahedra [37]. The x-ray photoemission spectra and cluster model analysis indicate the strongly hybridization between the d orbitals of Co^{3+} ions and p orbitals of O^{2-} ions [38]. The change of the phonon spectra with temperature can be quantitatively understood by the IS model with the orbital ordering [16]. The phonon mode appearing in the Raman scattering at room temperature is interpreted as the mode corresponding to the dynamical Jahn-Teller distortion [17]. Figure 1.10(a) shows the magnetic susceptibility of $LaCoO_3$ and the fitting curves [16]. For the analysis of the magnetization, the energy gap between the IS(HS) and LS Co^{3+} ions and the magnetic interaction between the IS(HS) Co^{3+} ions are taken into account. The evaluated IS Co^{3+} content as shown in Fig. 1.10(b) is over 0.8 at room temperature, which can be also quantitatively explained the temperature dependence of the infrared spectra [16]. We should note that the evaluated HS Co^{3+} content from the magnetization shown in Fig. 1.10(b) is quite different from that evaluated from the magnetization shown in Fig. 1.7(b). The difference between them are due to that the two different models are used for the analysis of the magnetization. which implies that the quantitative analysis of the magnetization for $LaCoO_3$ is difficult.

1.4 Non-magnetic-ion substitution effect for $LaCoO_3$

The spin state of Co^{3+} ions can be also changed by applying the external perturbation. For example, because the crystal field splitting are determined by the distance between the cation and ligand anion, the spin state of Co^{3+} ions is sensitive to the volume of the CoO_6 octahedra. The substitution for the large and small ions induce the lattice expansion and shrinking, which makes the crystal field splitting smaller and larger, respectively. The spin-state crossover is thus expected to be sensitive to the chemical substitution. As for the Fe(II) complex $Fe(phen)_2(NCS)_2$, the substitution effects are consistent with that expected from the chemical pressure [39]; the content of the HS Fe^{2+} ions decreases or increases by the substitution when the ionic radii of the substituted ions are smaller or larger than that of Fe^{2+} ions, respectively. When the cooperative effects are important for the spin-state crossover phenomena, the chemical substitution effects can be complicated.

Table 1.1: Effective ionic radius of M^{3+} ion (M = Al, Co, Ga, Rh) [40].

Ion	Al^{3+}	LS Co^{3+}	HS Co^{3+}	Ga^{3+}	Rh^{3+}
Effective ionic radius ($Å^2$)	0.535	0.545	0.61	0.62	0.665

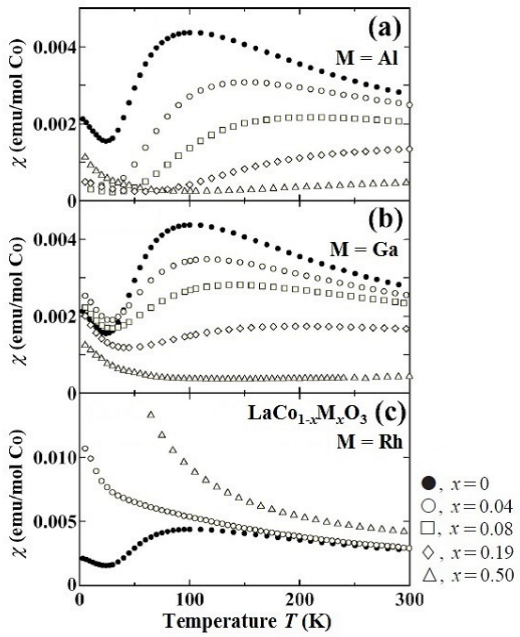

Figure 1.11: Magnetic susceptibility of $LaCo_{1-x}M_xO_3$ (M=Al, Ga, Rh) [11].

Figure 1.11 shows the magnetic susceptibility of $LaCo_{1-x}M_xO_3$ (M=Al, Ga, Rh) taken in 1 T [11]. We should note the Rh^{3+} ions ($4d^6$) prefer to take the LS state owing to its wide $4d$ orbitals inducing the large crystal field splitting. For M = Al and Ga, the magnetic susceptibility decreases by the substitution more drastically than expected from the dilution effect as shown in Fig. 1.11(a) and Fig. 1.11(b). In contrast, the spin-state crossover is not observed in the magnetic susceptibility and a Curie-Weiss like magnetization is stabilized down to the lowest temperature by 4% Rh substitution, as shown in Fig. 1.11(c). We should emphasize that these substitution effects cannot be explained by the chemical pressure. The effective ionic radii of M^{3+} ion (M = Al, Co, Ga, Rh) are listed in Table 1.1. The ionic radii of Ga^{3+} and Rh^{3+} ions are larger than that of Co^{3+} ions, and the lattice volume increases by the substitution [11], which indicates that the substitution for Ga^{3+} and Rh^{3+} ions give the negative chemical pressure. However, the Ga and Rh substitution effects on the magnetic properties are qualitatively different. Kyomen *et al.* proposed that these substitution effects can be explained based on the HS-LS model. They proposed that Rh^{3+} ions attract the ligand O^{2-} ions owing to the stronger covalency with the O^{2-} ions than that of Co^{3+} ions and stabilize the nearest neighbor Co^{3+} ions to HS state. Whereas, Al^{3+} and Ga^{3+} ions stabilize the Co^{3+} ions to LS state for the weaker covalency. According to this model, the direction of the displacement for O^{2-} ions are determined by the

electronic interaction. The Rh substitution effect on the spin state of Co^{3+} ions is still controversial. Li *et al.* proposed that Rh substitution makes the Co^{2+} and Rh^{4+} ions in $LaCoO_3$ in the similar way to Mn substitution [41] from the structural analysis [42]. In contrast to the significant change of the magnetic properties, the electrical resistivity and Seebeck coefficient are robust for the Ga and Rh substitution effects [43,44], which indicates that these substitution effects are local and static. First-principle calculations indicates that the unfilled $4d$ shell and covalency of Rh^{3+} ions stabilize the HS Co^{3+} ions, and that the substituted Rh^{3+} ions form the cluster owing to the elastic interaction [43]. Rh substitution affects the valence and spin state of Co^{3+} ions in the other cobalt oxides. In the layered cobalt oxide $Bi_2SrCo_2O_y$, the substituted Rh ions takes the higher valence state than the Co^{3+} ions [45]. For $La_{0.8}Sr_{0.2}CoO_3$, Rh substitution rapidly reduces the IS Co^{3+} ions [46].

Chapter 2

Spin state of Co^{3+} ions and its crossover phenomena in $LaCo_{1-x}Rh_xO_3$ investigated by structural properties

2.1 Introduction

In this chapter, we show the structural properties of $LaCo_{1-x}Rh_xO_3$. As shown in the previous chapter, the spin-state crossover induces the additional thermal expansion, which can be observed in the lattice volume as a function of temperature. The CoO_6 octahedron has the information about the Co^{3+} ions because the distortion of the octahedron depends on the spin state of Co^{3+} ions. We investigate the structural properties of $LaCo_{1-x}Rh_xO_3$ in order to discuss the spin state of Co^{3+} ions and its crossover phenomena. Here we choose the Rhodium for the substituted ions because of the simple magnetic behaviors shown in Chapter 3, which enable us to discuss the magnetization quantitatively. We first investigate the Rh content and temperature dependence of the lattice constants and volume by using the x-ray diffraction in order to discuss the spin-state crossover of Co^{3+} ions in Rh substituted samples. We have found the inhomogeneous change of the crystal structure from that with $R\bar{3}c$ to that with *Pnma* at around $x = 0.2$. It allows us to discuss the distortion of the CoO_6 octahedron without the restriction from the crystal symmetry because the orthorhombic *Pnma* structure has two inequivalent sites and allows the static Jahn-Teller distortion in the similar way to $LaMnO_3$ [47]. We thus discuss the spin state of Co^{3+} ions in $LaCo_{0.8}Rh_{0.2}O_3$ via the shape of the $Co(Rh)O_6$ octahedron, determined by powder neutron diffraction measurement.

2.2 Experiment

Polycrystalline samples of $LaCo_{1-x}Rh_xO_3$ ($0 \leq x \leq 0.9$) were prepared by a conventional solid-state reaction. A mixture of La_2O_3 ($3N$), Co_3O_4 ($3N$), and Rh_2O_3 ($3N$) with stoichiometric molar ratios was ground and calcined for 24 hour at 1000 °C in air. The calcined powder was ground, pressed into a pellet, and sintered for 48 hour at 1200 °C in air. These pellets were cooled slowly down to room temperature in the furnace by switching off the power after sintering. These samples were characterized by x-ray diffraction measured with Rigaku 4037V (Cu Kα radiation), and no impurity phases were detected. The oxygen contents of $LaCo_{1-x}Rh_xO_3$ for $x = 0, 0.2, 0.4, 0.6$ were determined by the thermogravimetric H_2 reduction analysis at laboratory of inorganic chemistry, Aalto university, Finland. The synchrotron powder x-ray diffraction for $LaCo_{0.9}Rh_{0.1}O_3$ and $LaCo_{0.8}Rh_{0.2}O_3$ were carried out at BL-8A and BL-8B, Photon Factory, KEK, Japan. We selected the wavelengths of 0.7755 Å and 0.6884 Å for the measurements from 100 to 300 K (BL-8A) and from 30 to 100 K (BL-8B), respectively. The diffraction patterns were analyzed by the Rietveld refinement using RIETAN-FP [48]. Neutron powder diffraction for $LaCo_{0.8}Rh_{0.2}O_3$ was carried out at 10 K at iMATERIA, MLF, J-PARC, Japan. The obtained diffraction pattern was analyzed by Z-Rietveld 0.9.37.2 [49, 50].

2.3 Results and Discussion

2.3.1 X-ray diffraction of $LaCo_{1-x}Rh_xO_3$

The oxygen contents $3 + \delta$ of $LaCo_{1-x}Rh_xO_{3+\delta}$ determined by the thermogravimetric reduction experiment are listed in Table 2.1. Except for $LaCoO_3$, the oxygen contents are little smaller than the stoichiometric oxygen content value. These value of Rh substituted samples are almost same as those obtained for the $La_{0.8}Sr_{0.2}Co_{1-x}Rh_xO_{3+\delta}$ system [46], which indicates only a tiny deviation from the stoichiometric oxygen content value. We also investigate the valence and spin state of Co and Rh ions in $LaCo_{1-x}Rh_xO_3$ by the x-ray absorption spectra, and conclude that the Co and Rh ions are trivalent and that Rh^{3+} ions take the LS state, as shown in the appendix A-1. In the following, we denote the samples with their stoichiometric oxygen-content value.

CuKα x-ray diffraction patterns for $LaCoO_3$ and $LaCo_{0.7}Rh_{0.3}O_3$ are in-

Table 2.1: Oxygen content of $LaCo_{1-x}Rh_xO_{3+\delta}$.

x	0	0.2	0.4	0.6
Oxygen content	3.02	2.95	2.94	2.93

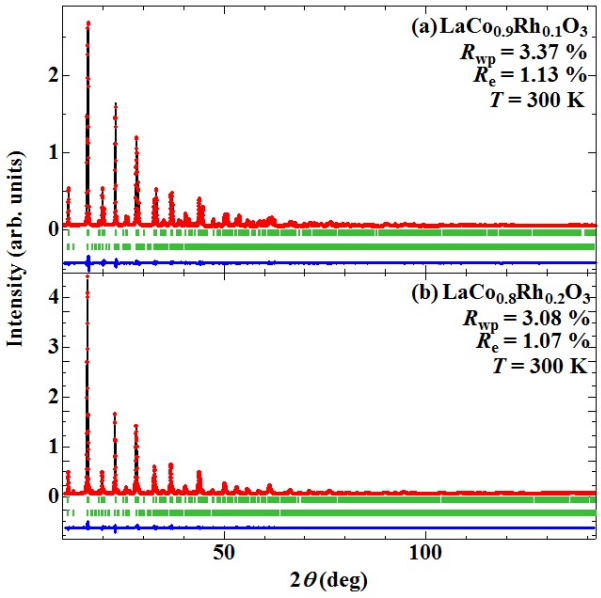

Figure 2.1: Synchrotron powder x-ray diffraction patterns for (a) $LaCo_{0.9}Rh_{0.1}O_3$ and (b) $LaCo_{0.8}Rh_{0.2}O_3$ at 300 K. The solid circle and solid line above the vertical bars represent the observed pattern, calculated pattern, respectively. Upper and lower vertical bars in the middle show the position of the Bragg peaks for the $R\bar{3}c$ and *Pnma* phases, respectively. The solid line below the vertical bars shows the difference curve.

dexed as $R\bar{3}c$ and *Pnma*, which indicates that there is the boundary between the rhombohedral $R\bar{3}c$ and orthorhombic *Pnma* in the phase diagram of $LaCo_{1-x}Rh_xO_3$. The x-ray diffraction patterns of $LaCo_{1-x}Rh_xO_3$ for $x \geq 0.4$ are indexed as *Pnma* phase, which is consistent with the experimental result that $LaRhO_3$ has the *Pnma* structure [51]. Figure 2.1 (a) and (b) show the synchrotron powder x-ray diffraction patterns for $LaCo_{0.9}Rh_{0.1}O_3$ and $LaCo_{0.8}Rh_{0.2}O_3$ at 300 K, respectively. No impurity phase is detected. We have analyzed these patterns as a mixture of two phases, $R\bar{3}c$ and *Pnma*, because these materials are located near the phase boundary.

X-ray diffraction patterns for $LaCo_{0.9}Rh_{0.1}O_3$ at 100, 180, 240, and 300 K are shown in Fig. 2.2. The patterns at 300 K shows two peaks, which are indexed as the (220) and (208) peaks of $R\bar{3}c$. Another peak, which cannot be indexed as $R\bar{3}c$, develops near 33 deg with decreasing temperature. This peak is indexed as the (242) peak in the *Pnma* phase, which indicates that the volume fraction of the *Pnma* phases increases with decreasing temperature. We thus analyzed the volume fraction as a function of temperature by fitting the diffraction patterns with the two phase mixture.

Figure 2.3(a) shows the lattice volume per formula unit of $LaCo_{1-x}Rh_xO_3$ as a function of the Rh content. The lattice volume increases with increasing

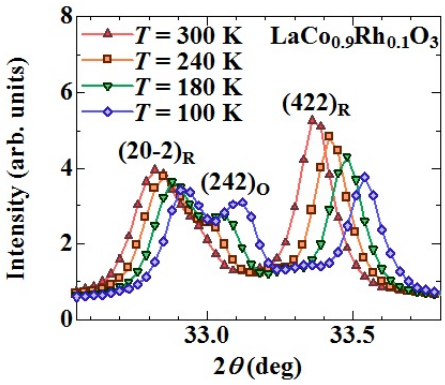

Figure 2.2: X-ray diffraction patterns for $LaCo_{0.9}Rh_{0.1}O_3$ at 100, 180, 240 and 300 K. $(20\text{-}2)_R$ and $(422)_R$ represent the (20-2) and (422) peaks of the $R\bar{3}c$ phase, and $(242)_O$ does the (242) peak of the *Pnma* phase.

the Rh content x, which is consistent with the previous study [42]. The lattice volume is larger than that expected from Vegard's law as shown by the broken line in Fig. 2.3 (a), which indicates that the Rh ions are not simply substituted for Co^{3+} ions in terms of the crystal structure. We should note that the Rh content in the sintered samples are roughly equal to the nominal content x, judging from the thermogravimetric analysis, x-ray absorption spectra, and synchrotron x-ray diffraction measurements. Therefore the deviation from Vegard's law is intrinsic. For $x = 0.1$ and 0.2, the lattice volume of the *Pnma* phase is larger than that of the $R\bar{3}c$ phase in the same composition. Lattice parameters of $LaCo_{1-x}Rh_xO_3$ as a function of Rh content are shown in Fig. 2.3(b). The rhombohedral angle α of the $R\bar{3}c$ phase for $LaCo_{1-x}Rh_xO_3$ increases from 60.8 to 61.2 deg as Rh content x increases from 0 to 0.2. The change of the lattice parameters for *Pnma* phase are different from each other, which is consistent with the previous study [42].

Figure 2.4 shows the temperature dependence of the volume fraction of the $R\bar{3}c$ phase for $LaCo_{0.9}Rh_{0.1}O_3$ and $LaCo_{0.8}Rh_{0.2}O_3$. The volume fraction of the $R\bar{3}c$ phase decreases with increasing x or with decreasing temperature, suggesting that the crystal structure inhomogeneously changes from the $R\bar{3}c$ to *Pnma* phase as a function of Rh content and temperature as a mixed phase. Similar structural change and phase mixture are also observed in $La_{1-x}Ca_xCoO_3$ [52]. Ca substitution for La and Rh substitution for Co similarly decrease the tolerance factor of $LaCoO_3$, which suggests that the origin of the inhomogeneously changes of the crystal structure in $LaCo_{1-x}Rh_xO_3$ is the lattice distortion caused by the substituted Rh^{3+} ions.

Figure 2.5(a) shows the lattice volume of $LaCo_{0.9}Rh_{0.1}O_3$ and $LaCo_{0.8}Rh_{0.2}O_3$ as a function of temperature together with the temperature dependence of the lattice volume for $LaCoO_3$ reported by K. Asai *et al* [12]. The lattice volume

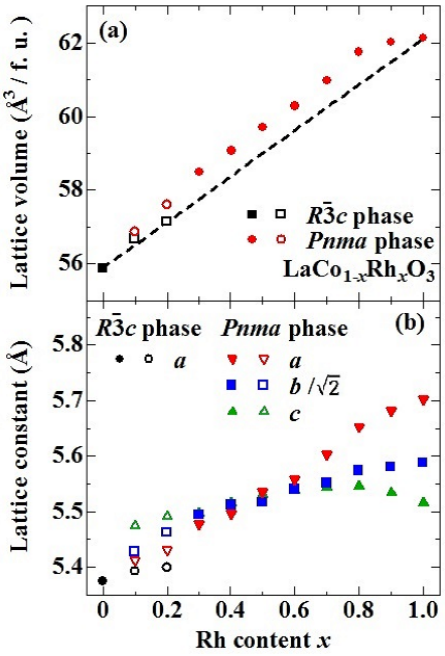

Figure 2.3: (a) Lattice volume per formula unit of $LaCo_{1-x}Rh_xO_3$ as a function of the Rh content. A broken line represents the change of the lattice volume expected from Vegard's law. Solid and open symbols represent the experimental data evaluated from the CuKα and synchrotron x-ray diffraction, respectively. (b) Lattice parameters of $LaCo_{1-x}Rh_xO_3$ as a function of Rh content. Solid and open symbols represent the experimental data evaluated from the CuKα and synchrotron x-ray diffraction, respectively.

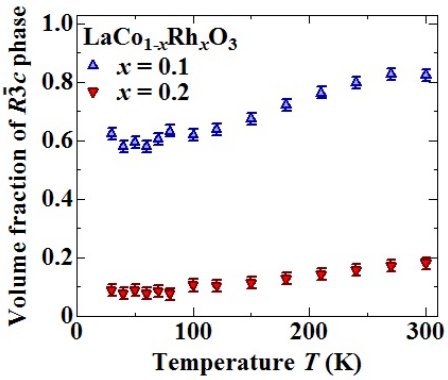

Figure 2.4: Temperature dependence of the volume fraction of the $R\bar{3}c$ phase of $LaCo_{0.9}Rh_{0.1}O_3$ and $LaCo_{0.8}Rh_{0.2}O_3$.

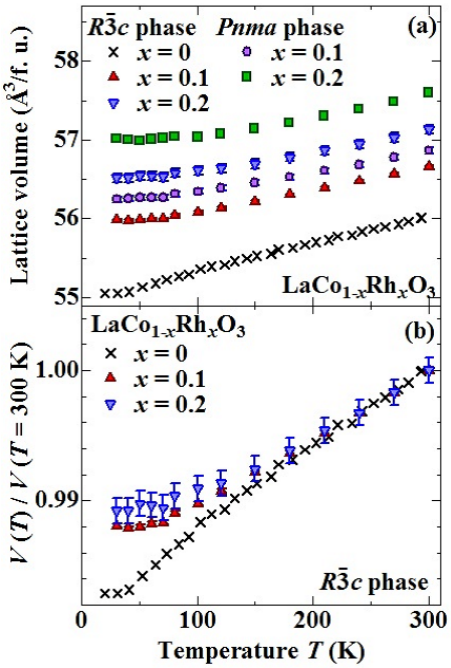

Figure 2.5: (a)Temperature dependence of the lattice volume of $LaCo_{0.9}Rh_{0.1}O_3$ and $LaCo_{0.8}Rh_{0.2}O_3$. The temperature dependence of the lattice volume for $LaCoO_3$ taken from Ref. [12] is also plotted. (b)Temperature dependence of the lattice volume normalized by V(300 K) for $R\bar{3}c$ phase of $LaCo_{1-x}Rh_xO_3$ for $x = 0, 0.1, 0.2$.

of two phases for Rh substituted samples similarly changes as a function of temperature. Figure 2.5(b) shows the temperature dependence of the lattice volume normalized by the value at 300 K for the $R\bar{3}c$ phase of $LaCo_{1-x}Rh_xO_3$ for $x = 0, 0.1, 0.2$. As shown in section 1.2.1, the lattice volume of $LaCoO_3$ continues to decrease with decreasing temperature down to 40 K and that the thermal expansion coefficient of $LaCoO_3$ enhances owing to the spin-state crossover. The lattice volume of $LaCo_{0.9}Rh_{0.1}O_3$ and $LaCo_{0.8}Rh_{0.2}O_3$ decreases with the thermal expansion coefficient similar to that of $LaCoO_3$ from room temperature, and ceases to decrease around 70 K. It shows that Rh^{3+} substitution suppresses the spin-state crossover below 70 K, and indicates that the HS Co^{3+} content increases with increasing temperature in Rh^{3+} substituted samples.

2.3.2 Powder neutron diffraction of $LaCo_{0.8}Rh_{0.2}O_3$

Figure 2.6 shows the neutron diffraction pattern for $LaCo_{0.8}Rh_{0.2}O_3$ at 10 K. We can see the small (222) peak of the $R\bar{3}c$ phase in the profile, which is shown in the inset of Fig. 2.6. Thus we can analyze the profile as a mixture

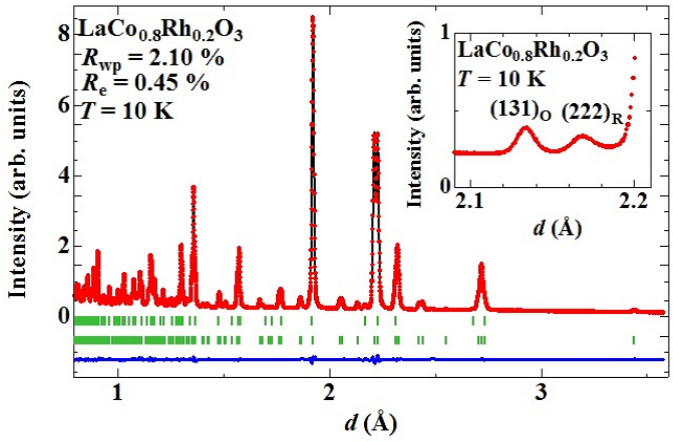

Figure 2.6: Neutron diffraction pattern for $LaCo_{0.8}Rh_{0.2}O_3$ at 10 K. The solid circle and solid line above the vertical bars represent the observed pattern, calculated pattern, respectively. Upper and lower vertical bars in the middle show the position of the Bragg peaks for the $R\bar{3}c$ and *Pnma* phases, respectively. The solid line below the vertical bars shows the difference curve. The inset shows the pattern for $2.09 \leq d \leq 2.21$ Å. $(222)_{\rm R}$ and $(131)_{\rm O}$ represent the (222) and (131) peaks of the $R\bar{3}c$ and *Pnma* phase, respectively.

Table 2.2: Structural parameters of $LaCo_{0.8}Rh_{0.2}O_3$ from the neutron diffraction at 10 K.

Atom	Site	x	y	z	B (Å^2)
La	4c	0.4753(2)	0.25	0.5039(1)	0.07(5)
Co(Rh)	4b	0	0	0.5	0.18(1)
O1	4c	0.004(1)	0.25	0.4336(5)	0.35(1)
O2	8d	0.2232(2)	0.0353(1)	0.7761(1)	0.35(1)

of $R\bar{3}c$ and *Pnma* phases, and evaluate the volume fraction to be 3 % for the $R\bar{3}c$ phase from the analysis, which is consistent with the experimental results shown in Fig. 2.4. We will not discuss the crystal structure for the $R\bar{3}c$ phase because the small volume fraction makes it difficult to evaluate the structural parameters of the $R\bar{3}c$ phase. For the *Pnma* phase, the lattice parameters a = 5.4125(6) Å, b = 7.7002(6) Å, and c = 5.4739(2) Å are evaluated from the neutron diffraction pattern shown in Fig. 2.6.

Table 2.2 lists the structural parameters of $LaCo_{0.8}Rh_{0.2}O_3$. The z position of O1 is different from the previous study [42]. We should emphasize that our structural analysis based on the neutron diffraction can determine the position of the oxygen more accurately than that of the previous study based on the CuKα x-ray diffraction pattern. Table 2.3 list the bond lengths

Table 2.3: Evaluated bond lengths and bond angles of $LaCo_{0.8}Rh_{0.2}O_3$. M = Co(Rh).

Bond length (Å)		Bond angle (deg)	
M-O1 × 2	1.9592(6)	M-O1-M × 2	158.57(15)
M-O2 × 2	1.9540(9)	M-O2-M × 4	159.99(2)
M-O2 × 2	1.9545(6)	O1-M-O2 × 2	90.00(3)
		O1-M-O2 × 2	90.68(2)
		O2-M-O2 × 2	91.75(1)

and bond angles of $LaCo_{0.8}Rh_{0.2}O_3$. The evaluated Co(Rh)-O bond length have almost isotropic values, indicating that there is no static Jahn-Teller distortion. A small difference in the bond lengths is possible even when the containing transition metal ion is not Jahn-Teller active. For example, The difference in Rh-O bond lengths for $LaRhO_3$ is evaluated to be 0.025(6) Å [51], which is much larger than that evaluated from Table 2.3. It indicates that the evaluated difference in the Co-O bond lengths is negligible. Let us discuss the spin state of the Co^{3+} ion quantitatively through the shape of the $Co(Rh)O_6$ octahedron. In contrast to the HS and LS Co^{3+} ion, the IS Co^{3+} ion has the Jahn-Teller instability at the e_g orbitals. The Co-O bond lengths thus will be anisotropic when the CoO_6 octahedron contains the IS Co^{3+} ion. On the other hand, when the CoO_6 octahedron contains the HS or LS Co^{3+} ion, the bond lengths are expected to be identical. In order to discuss the distortion of the $Co(Rh)O_6$ octahedra in $LaCo_{0.8}Rh_{0.2}O_3$, we simply assume that the regular RhO_6 octahedra dilutes the distortion of the CoO_6 octahedron. If the Jahn-Teller distortion as shown in Fig. 1.9 also occurred in $LaCo_{0.8}Rh_{0.2}O_3$, we could evaluate the diluted distortion from our structural analysis. Two inequivalent sites of oxygen ions in *Pnma* phase enable us to evaluate the difference in the Co-O bond lengths without the restriction from the the crystal symmetry, which is in remarkable contrast to the case of $LaCoO_3$, where all the oxygen sites are equivalent and the Co-O bond lengths must be isotropic. The difference in the Co-O bond lengths is evaluated to be 0.005 Å from the bond lengths given in Table 2.3, which is 3 % of that of the CoO_6 octahedron containing the IS Co^{3+} ion which is reported for $Sr_3YCo_4O_{10.5+\delta}$ (0.15 Å) [53]. Taking the dilution effect of the substituted Rh^{3+} ions into account, we conclude that the content of the IS Co^{3+} ions is less than 4% from the structural point of the view, which is quite different from the IS Co^{3+} content shown in the section 1.3.2. The HS-LS model can naturally explain the shape of the $Co(Rh)O_6$ octahedron. We should note the orbital degree of freedom for Co^{3+} ions which can induce dynamical Jahn-Teller distortion. If the Co^{3+} ions have the orbital degree of freedom which induces the Jahn-Teller distortion, the structural phase transition must occur owing to quench the degree of the freedom at the lowest temperature in the similar way to $LaMnO_3$ [47]. In our structural analysis, no structural phase transition accompanied by the

Jahn-Teller distortion is observed for $LaCo_{0.8}Rh_{0.2}O_3$, which suggests that the Co^{3+} ions in $LaCo_{0.8}Rh_{0.2}O_3$ have no orbital degree of the freedom.

Next, let us discuss the volume V_{obs} of the $Co(Rh)O_6$ octahedron in $LaCo_{0.8}Rh_{0.2}O_3$. Now V_{obs} can be regarded as the average of the volume for octahedra which have the HS Co^{3+}, LS Co^{3+}, and Rh^{3+} ions. We can thus calculate the volume by using the following equation,

$$V_{cal} = 0.8V_{LCO} + 0.2V_{LRO}. \tag{2.1}$$

V_{LCO} and V_{LRO} represent the volume of the CoO_6 octahedron in $LaCoO_3$ and that of the RhO_6 octahedron in $LaRhO_3$, respectively. V_{LCO} is evaluated from the structural parameters of $LaCoO_3$ [14]. V_{LRO} is set to be 11.54 Å^3 estimated from the x-ray diffraction at 294 K [51] because no structure data are available for $LaRhO_3$ at low temperatures. V_{obs} is determined to be 9.97 Å^3 by using the structural parameters given in Table 2.3. We first calculate V_{cal} for the LS Co^{3+} ions. When V_{LCO} (= 9.51 Å^3) is taken from the structural parameters at 10 K, we get V_{cal} = 9.92 Å^3, which is substantially smaller than V_{obs}. It indicates that there are HS Co^{3+} ions in $LaCo_{0.8}Rh_{0.2}O_3$. V_{obs} is close to V_{cal} when the structural parameters of $LaCoO_3$ at 150 K are used for the calculation (V_{LCO} = 9.58 Å^3). The temperature of 150 K is substantially higher than that at which the spin-state crossover of Co^{3+} ions in $LaCoO_3$ takes place. It indicates that the spin-state crossover is suppressed in $LaCo_{0.8}Rh_{0.2}O_3$, which is consistent with the temperature dependence of the lattice volume for $LaCo_{0.8}Rh_{0.2}O_3$.

2.3.3 HS Co^{3+} content evaluated by the lattice volume

In this section, we roughly evaluate the HS Co^{3+} content from the lattice volume as shown in Fig. 2.3(a) and 2.5(a) in order to discuss the spin state of Co^{3+} ions for $LaCo_{1-x}Rh_xO_3$ as a function of temperature and Rh content more quantitatively. Here we regard HS and LS Co^{3+} ions as two different species of ions having their unique ionic radii, and assume a homogeneous solid solution consisting of HS Co^{3+}, LS Co^{3+}, and Rh^{3+} in the Co(Rh) sites of $LaCo_{1-x}Rh_xO_3$. We cannot discuss the local distortion induced by Rh^{3+} ions in this analysis because the lattice volume is evaluated as an averaged crystal structure. We first evaluate the contribution to the spin-state crossover for the thermal lattice expansion by subtracting the other contributions from the experimental results. We calculate the temperature dependence of the lattice volume for $LaCoO_3$ expected from the phonon contribution by using the Grüneisen-Einstein formula, which is derived in the section 1.2.1. V(0 K) (= 55.06 Å^3) is evaluated by extrapolating the lattice volume of $LaCoO_3$ shown in Fig. 2.5(a) towards 0 K. The exact value of T_E and α_V for $LaCoO_3$ cannot be evaluated from the experimental results of this material because of the spin-state crossover. T_E and α_V rapidly decreases by suppression of the spin-state crossover, for example, by Sr substitution for La [54]. Because these

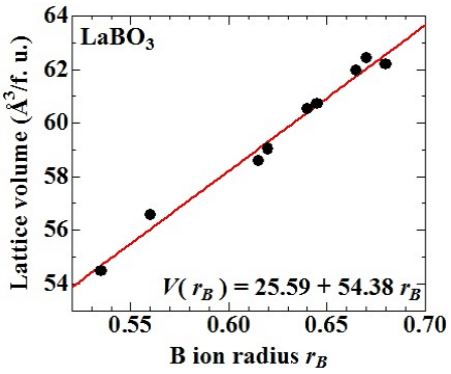

Figure 2.7: Lattice volume of $LaBO_3$ listed in Ref. [14] as a function of the ionic radius for B ions.

parameters of $La_{1-x}Sr_xCoO_3$ are independent of the Sr content above $x = 0.2$, we use T_E and α_V of 142 K and 2.76×10^{-5} K^{-1} for $La_{0.7}Sr_{0.3}CoO_3$, respectively. Next, we assume that the lattice also expands through the increase of an average ionic radius for Co(Rh) sites (B sites) as reported in the previous study [14]. We can obtain the additional lattice expansion ΔV_B due to the HS Co^{3+} and Rh^{3+} ions as

$$\Delta V_B = \Delta r_B \frac{\partial V}{\partial r_B} = x_B(r_B - r_{LS})\frac{\partial V}{\partial r_B}, \tag{2.2}$$

where x_B and r_B represent the content and ionic radius of B ions, respectively. As for the B ion, we abbreviate HS Co^{3+}, LS Co^{3+}, and Rh^{3+} to HS, LS, and Rh, respectively. Finally we obtain the expression for the lattice volume of Rh substituted samples given by

$$V(T) = V_{GE}(T) + \Delta V_{Rh} + \Delta V_{HS}(T). \tag{2.3}$$

For $x = 0.1$ and 0.2, we evaluate $V(T)$ as an average of two phases from the lattice volume and volume fraction of the two phases evaluated from the synchrotron x-ray diffraction measurements. We use the experimental results shown in Fig. 2.3(a) as V(300 K) for the other composition. $\partial V/\partial r_B$ is evaluated to be 54.38 $Å^2$ from the lattice volume of $LaBO_3$ as a function of the ionic radius for B ions shown in Fig. 2.7. The values of r_B for B = LS, HS, and Rh are set to be 0.545, 0.61, and 0.665 Å, respectively [40]. Now we can calculate ΔV_{Rh} by using x_{Rh} taken from the chemical formula of the samples.

Figure 2.8(a) shows the contributions of $V_{GE}(T)$ and ΔV_{Rh} together with $V(T)$ for $LaCo_{0.8}Rh_{0.2}O_3$. Now we can evaluate the $\Delta V_{HS}(T)$ by subtracting $V_{GE}(T)$ + ΔV_{Rh} from $V(T)$. Figure 2.8(b) shows the temperature dependence of HS Co^{3+} content x_{HS} evaluated from $\Delta V_{HS}(T)$ of $LaCo_{1-x}Rh_xO_3$ for $0 \leq x \leq 0.2$. x_{HS} at room temperature for $LaCoO_3$ is around 0.2, which is

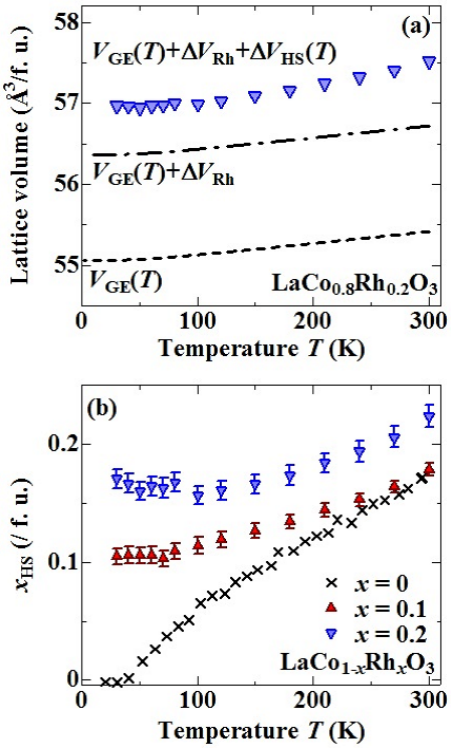

Figure 2.8: (a)The lattice volume of $LaCo_{0.8}Rh_{0.2}O_3$ for a mixture of two phases as a function of temperature. The dotted and dot-dashed lines represent $V_{\rm GE}(T)$ and $V_{\rm GE}(T)$ + $\Delta V_{\rm Rh}$ evaluated for $LaCo_{0.8}Rh_{0.2}O_3$, respectively (see text). (b)The content of the HS Co^{3+} ions for $LaCo_{1-x}Rh_xO_3$ for $0 \leq x \leq 0.2$ as a function of temperature.

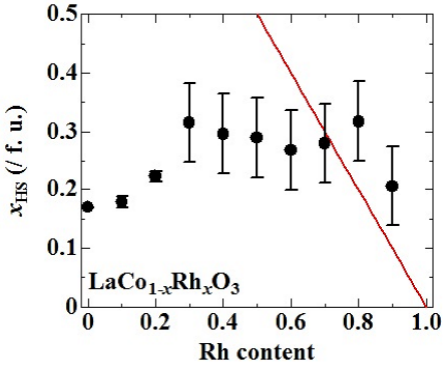

Figure 2.9: The content of the HS Co^{3+} ions at room temperature for $LaCo_{1-x}Rh_xO_3$ for $0 \leq x \leq 0.9$ as a function of Rh content. The solid line represents the content of Co^{3+} ions expected from the chemical formula.

consistent with the previous study [31, 32]. $x_{\rm HS}$ of $LaCoO_3$ decreases to zero with decreasing temperature owing to the spin-state crossover. On the other hand, $x_{\rm HS}$ for Rh^{3+} substituted samples decreases from room temperature, and ceases to decrease below 70 K. 15% Co^{3+} ions in $LaCo_{0.8}Rh_{0.2}O_3$ are stabilized as HS state down to lowest temperature. The temperature dependence of $x_{\rm HS}$ for $LaCo_{1-x}Rh_xO_3$ cannot be explained by the thermal excitation. We leave microscopic mechanism of the temperature dependence for $x_{\rm HS}$ open, because we simply assume the solid solution of HS Co^{3+}, LS Co^{3+}, and Rh^{3+} ions. The HS Co^{3+} content $x_{\rm HS}$ at room temperature for $LaCo_{1-x}Rh_xO_3$ for $0 \leq x \leq 0.9$ as a function of Rh content is shown in Fig. 2.9. The evaluated $x_{\rm HS}$ above $x \geq 0.8$ exceeds the Co^{3+} content expected from the chemical formula, which is due to that the large $\Delta V_{\rm Rh}$ in addition to the large experimental error makes it difficult to evaluate $\Delta V_{\rm HS}(T)$. $x_{\rm HS}$ at room temperature is almost independent of Rh content, which is not expected from the simple dilution effect. It indicates that Rh^{3+} substitution preferentially reduce LS Co^{3+} ions at room temperature.

2.4 Summary

We have carried out the CuKα x-ray diffraction for polycrystalline samples of $LaCo_{1-x}Rh_xO_3$ for $0 \leq x \leq 0.9$, synchrotron powder x-ray diffraction for $LaCo_{0.9}Rh_{0.1}O_3$ and $LaCo_{0.8}Rh_{0.2}O_3$, and neutron powder diffraction for $LaCo_{0.8}Rh_{0.2}O_3$. The lattice volume as a function of Rh content has a positive deviation from the Vegard's law. The lattice volume of $LaCo_{0.9}Rh_{0.1}O_3$ and $LaCo_{0.8}Rh_{0.2}O_3$ ceases to decrease around 70 K, which is different from the temperature dependence of the lattice volume for $LaCoO_3$. The thermal expansion coefficient at room temperature is almost independent of the Rh content, which suggests that the HS Co^{3+} content increases with increasing temperature in the Rh substituted samples. The CoO_6 octahedra of $LaCo_{0.8}Rh_{0.2}O_3$ determined by the neutron diffraction are found to be isotropic, which supports the HS-LS model. The volume of the $Co(Rh)O_6$ octahedra of $LaCo_{0.8}Rh_{0.2}O_3$ (9.97 Å^3) is larger than that expected from the mixture of the LS Co^{3+} and Rh^{3+} ions, which indicates that the Rh substitution suppress the spin-state crossover. We evaluate the HS Co^{3+} content for $LaCo_{1-x}Rh_xO_3$ as a function of temperature and Rh content. The HS Co^{3+} content of Rh^{3+} substituted samples decreases with decreasing temperature as that of $LaCoO_3$ does at room temperature, and ceases to decrease below 70 K. The HS Co^{3+} content is almost independent of Rh content, which indicates that Rh substitution preferentially reduce the LS Co^{3+} content at room temperature.

Chapter 3

Weak ferromagnetism in $LaCo_{1-x}Rh_xO_3$ induced by the Rh substitution

3.1 Introduction

In this chapter, we show the magnetic properties of $LaCo_{1-x}Rh_xO_3$. In the previous chapter, we investigate the structural properties of $LaCo_{1-x}Rh_xO_3$, and finally evaluate the HS Co^{3+} content from the lattice volume. For $LaCoO_3$, the evaluated HS Co^{3+} content is consistent with that reported in the previous study. Rh substitution suppresses the spin-state crossover, and 15% of the Co^{3+} ions are stabilized as the high-spin state down to the lowest temperature. At room temperature, Rh substitution preferentially reduces the LS Co^{3+} content. Magnetization is more appropriate for the quantitative discussion on the spin state of Co^{3+} ions in $LaCo_{1-x}Rh_xO_3$. The most remarkable difference between the LS and HS Co^{3+} ions is the magnetic properties; the LS and HS Co^{3+} ion are non-magnetic (S = 0) and magnetic (S = 2), respectively. The HS Co^{3+} ions is only magnetic in the Rh substituted samples because Rh^{3+} ions are non-magnetic. We investigate the magnetic properties of $LaCo_{1-x}Rh_xO_3$ in order to discuss the spin state of Co^{3+} ions and Rh substitution effect more quantitatively. In this research, we have found a weak ferromagnetic ordering emerging in $0.1 \leq x \leq 0.4$ below 15 K. The ferromagnetic ordering is driven only by the HS Co^{3+} ions, which is different from the ferromagnetic ordering of $La_{1-x}Sr_xCoO_3$ occurring in the mixed valence state of Co^{3+} and Co^{4+} ions [35]. We should note that the magnetic ordering of Rh substituted samples is also different from that in a biaxially strained film of $LaCoO_3$ [27] because the crystal structure isotropically expands by Rh substitution. We further have measured the magnetization of $LaCo_{1-x}Rh_xO_3$ as a function of temperature, applied magnetic field, and time. We have carried out the neutron scattering measurements in order to discuss the magnetic ordering. Finally, we evaluate

the HS Co^{3+} content from the magnetization by modifying the Curie-Weiss law for the spin-state crossover system. We should emphasize that the evaluated HS Co^{3+} content is quantitatively consistent with that evaluated from lattice volume shown in Fig. 2.3.3.

3.2 Experiment

Polycrystalline samples of $LaCo_{1-x}Rh_xO_3$ ($0 \leq x \leq 0.9$) were prepared by a conventional solid-state reaction as shown in the section 2.2. A single crystal of $LaCo_{0.8}Rh_{0.2}O_3$ for the neutron scattering was grown by a floating zone method from a polycrystalline rod of $LaCo_{0.8}Rh_{0.2}O_3$ in an infrared-heating furnace (Crystalsystems, FZ-F4000-H-I-V). The polycrystalline rod with a 70-mm length and a 6-mm radius was prepared by a solid-state reaction method as shown in Section 2.2. We used a single crystal of $LaCoO_3$ as a seed rod in order to trigger crystal growth. The size of the obtained single crystal is a 10-mm long rod with a 4-mm radius. Magnetization in field cooling (FC) and zero field cooling (ZFC) processes were measured using a superconducting quantum interference device (SQUID) magnetometer (Quantum Design MPMS) from 5 to 300 K in an applied field of 1 T for the polycrystalline samples of $LaCo_{1-x}Rh_xO_3$. For $0.1 \leq x \leq 0.5$, low-field magnetization in FC and ZFC processes were also measured in 0.05 T. Magnetization-field (M - H) curves of $LaCo_{0.8}Rh_{0.2}O_3$ from 2 to 50 K were measured in sweeping $\mu_0 H$ from 0 to 7 T, and from 7 to 0 T. For the measurement of the isothermal remanent magnetization as a function of time, the samples was cooled from room temperature down to 5 K without a magnetic field. Then, a magnetic field was swept from 0 to 5 T, and from 5 to 0 T. Neutron scattering measurements were carried out on the triple-axis spectrometer ISSP-PONTA at JRR-3 of JAEA in Tokai. The 002 reflections of Pyrolytic graphite (PG) were used for both the monochromator and analyzer. The horizontal collimations

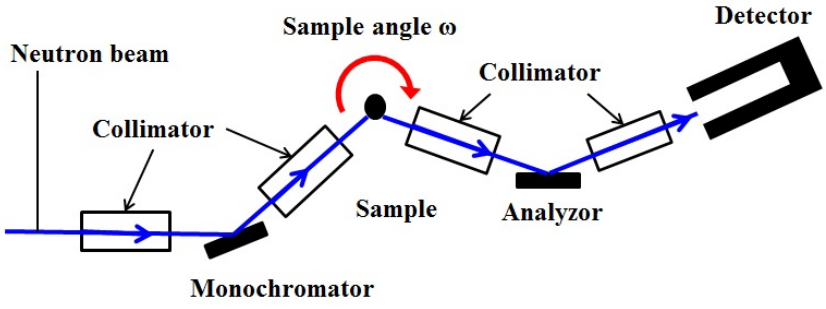

Figure 3.1: Schematic picture of the triple-axis spectrometer and the direction of the sample angle ω.

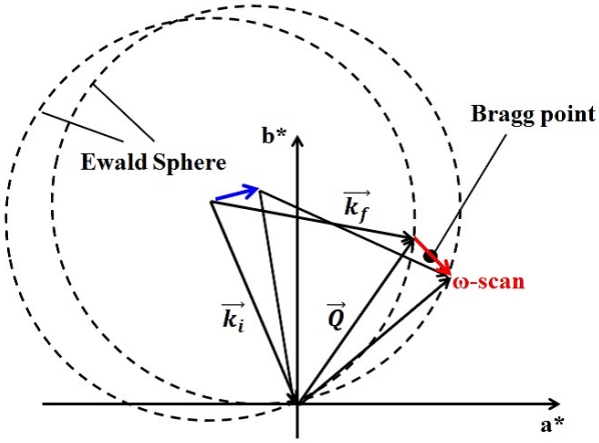

Figure 3.2: Schematic picture of the the sample-angle-scan (ω-scan) in the reciprocal lattice space. $\vec{k_i}$ and $\vec{k_f}$ represent the wave vectors of the incident and scattered neutron. $\vec{Q}$ represents the scattering vector. The origin is set to the starting point of the scattering vector. The angle between the two wave vectors and the radii of the two Ewald sphere are same.

were set to be 40'-80'-80'-80', and the neutron wavelength was 2.359 Å. PG filters were placed after the second collimator and after the sample to suppress the higher-order contamination. The crystal was set in an Al-can filled with helium gas, and the can was attached to the cold head of the Displex type refrigerator. We carried out the sample-angle-scan (ω-scan) at some Bragg points. Figure 3.1 shows the schematic picture of the triple-axis spectrometer and sample angle ω. In the ω-scan, the angle between the incident and scattered neutron beams are fixed in the Bragg condition, and the sample angle ω only changes. Thus, in the reciprocal lattice space, the scattering vector $\vec{Q}$ rotate with remaining $|\vec{Q}|$ in the scanning as shown in Fig. 3.2. The direction of the ω-scan is perpendicular to that of the $\omega - 2\theta$ scan in the reciprocal lattice space.

3.3 Results and Discussion

3.3.1 Magnetization of $LaCo_{1-x}Rh_xO_3$

Figure 3.3(a) and 3.3(b) show the temperature dependence of magnetization for $LaCo_{1-x}Rh_xO_3$ taken in 1 T. For $x = 0$, the magnetization decreases with decreasing temperature below 100 K except for the small upturn owing to the impurity contribution, which is known as the spin-state crossover. In contrast, the magnetization increases with decreasing temperature for all of the Rh substituted samples, which indicates that the spin-state crossover is sub-

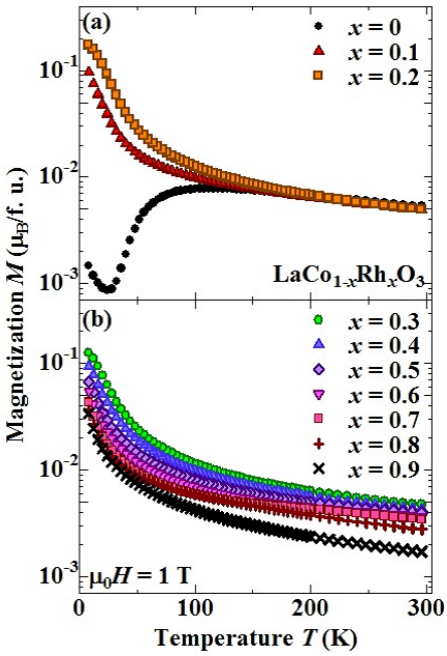

Figure 3.3: Temperature dependence of the magnetization for $LaCo_{1-x}Rh_xO_3$ taken in 1 T for (a) $0 \leq x \leq 0.2$ and (b) $0.3 \leq x \leq 0.9$, respectively.

stantially suppressed. It is consistent with the structural properties discussed in the previous chapter. The magnetization takes a maximum at $x = 0.2$ as a function of x below 150 K.

The temperature dependence of the magnetization for $LaCo_{1-x}Rh_xO_3$ taken in 0.05 T for $0.1 \leq x \leq 0.5$ is shown in Fig. 3.4. We can observe a hysteresis between the magnetization in FC and ZFC processes for $0.1 \leq x \leq 0.4$ below 15 K. Figure 3.5 shows the magnetization-field curve for $LaCo_{0.8}Rh_{0.2}O_3$. A hysteresis of magnetization with a spontaneous magnetization is observed at 2 K, which indicates the magnetic ordering. The magnetization does not saturate and increases linearly with increasing applied magnetic field above 6 T. We should emphasize that the magnetization at 7 T (0.35 μ_B per f. u. at 2 K) is much smaller than the magnetic moment of the Co^{3+} ion (4.0 μ_B for the HS Co^{3+} ion). It indicates that the magnetic ordering of $LaCo_{1-x}Rh_xO_3$ is the weak ferromagnetic ordering with the antiferromagnetic component and/or disordering. No magnetic peaks corresponding to the antiferromagnetic ordering was detected in the neutron scattering measurements shown below. A more detailed magnetic structure is to be explored for understanding the magnetization-field curve for $LaCo_{0.8}Rh_{0.2}O_3$.

Figure 3.6(a) and 3.6(b) show the magnetization of $LaCo_{0.8}Rh_{0.2}O_3$ and the applied magnetic field as a function of time, respectively. We set $t = 0$ to be

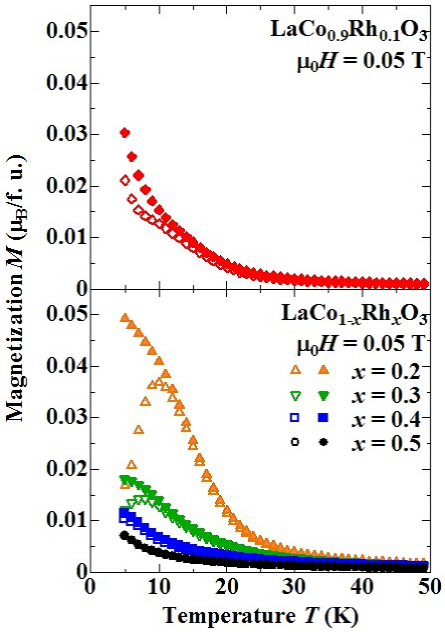

Figure 3.4: Temperature dependence of the magnetization for (a) $LaCo_{0.9}Rh_{0.1}O_3$ and (b) $LaCo_{1-x}Rh_xO_3$ for $0.2 \leq x \leq 0.5$ taken in 0.05 T. Solid and open symbols represent the magnetization in the FC and ZFC processes, respectively.

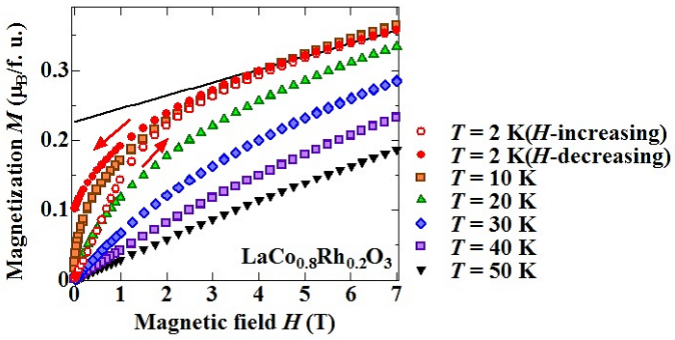

Figure 3.5: Magnetization-field curve for $LaCo_{0.8}Rh_{0.2}O_3$. The solid line represents the linear fit of the data at 2 K above 6 T.

the time when the applied magnetic field decreases down to 0 T. The spontaneous magnetization is observed for $t \geq 0$, which is consistent with the results shown in Fig. 3.5. Isothermal remanent magnetization of $LaCo_{1-x}Rh_xO_3$ for $0.1 \leq x \leq 0.3$ and that normalized by the value of the magnetization taken at $t = 0$ as a function of time are shown in Fig. 3.7(a) and Fig. 3.7(b), respectively. Remanent magnetization is observed for Rh substituted samples

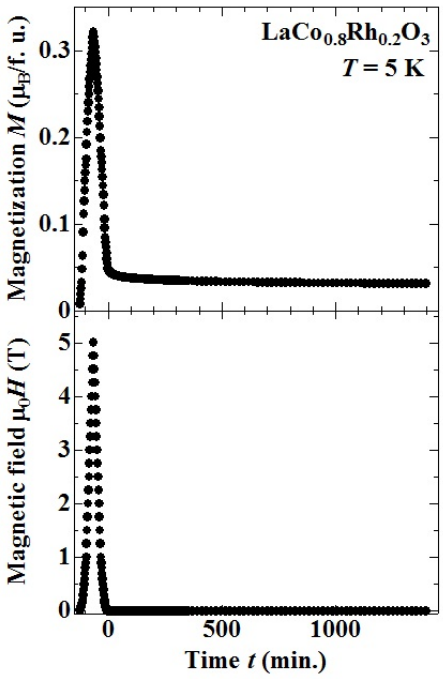

Figure 3.6: (a) Magnetization of $LaCo_{0.8}Rh_{0.2}O_3$ and (b) applied magnetic field as a function of time.

even though $LaCoO_3$ is non-magnetic at low temperature. The magnetization of $LaCo_{0.9}Rh_{0.1}O_3$ does not depend on the time at $t > 100$ min, which indicates that the long-range ferromagnetic ordering emerges at $x = 0.1$. In contrast, the magnetization of $LaCo_{0.8}Rh_{0.2}O_3$ and $LaCo_{0.7}Rh_{0.3}O_3$ decreases with increasing time. These experimental results suggest that Rh substitution disorders the long-range ferromagnetic ordering of $LaCo_{0.9}Rh_{0.1}O_3$. We should emphasize that the magnetization increases by Rh substitution from $x = 0.1$ to 0.2, which indicates that Rh substitution induces the magnetization at low temperature on one hand and disorders the magnetic ordering to make a glassy state on the other.

3.3.2 Weak ferromagnetic ordering of $LaCo_{1-x}Rh_xO_3$

In this section, we discuss the weak ferromagnetic ordering of $LaCo_{1-x}Rh_xO_3$ shown in the section 3.3.1. We first define the transition temperature of the magnetic ordering. As shown in Fig. 3.4, there is no obvious development of the magnetization for the transition. Instead, we define the ferromagnetic transition temperature T_C as the temperature at which $|dM/dT|$ takes a maximum in 0.05 T, as shown in Fig. 3.8(a). Figure 3.8(b) shows the transition temperature for $LaCo_{1-x}Rh_xO_3$ ($0 \leq x \leq 0.5$) as a function of Rh content x.

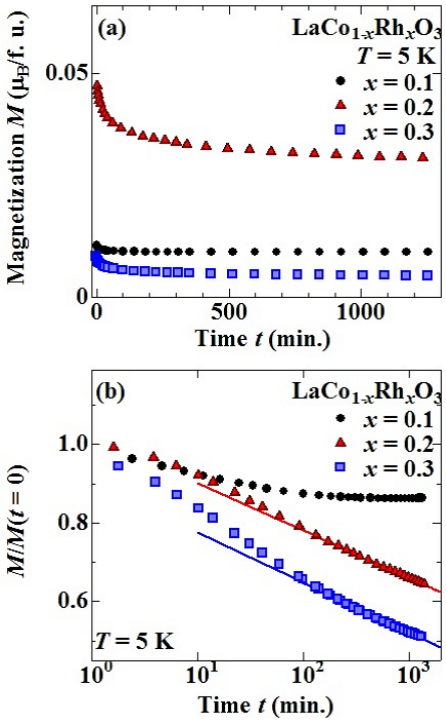

Figure 3.7: (a) Isothermal remanent magnetization of $LaCo_{1-x}Rh_xO_3$ for $0.1 \leq x \leq 0.3$ as a function of time. (b) Time dependence of the isothermal remanent magnetization of $LaCo_{1-x}Rh_xO_3$ for $0.1 \leq x \leq 0.3$ normalized by the value of the magnetization taken at t = 0 with the logarithmic axis. Solid lines shown in (b) represent the linear fit of the data for $t > 100$ min.

The ferromagnetic transition appears at $x = 0.1$, and the maximum T_C of 15 K is obtained at $x = 0.2$. T_C decreases with increasing Rh content for $x = 0.2$ and disappears at $x = 0.5$.

Next, we discuss the magnetization-field curve for $LaCo_{0.8}Rh_{0.2}O_3$ shown in Fig. 3.5. In order to separate the ferromagnetic component from the other, we fit the curves above 6 T linearly as shown by the solid line in Fig. 3.5. Then we can evaluate the saturation magnetization M_S and magnetic susceptibility $\Delta M/\Delta H$ from the intersection and slope of the fitted line, respectively. Figure 3.9(a) and 3.9(b) show the temperature dependence of M_S and $\Delta M/\Delta H$, respectively. The saturation magnetization gradually increases with decreasing temperature below 40 K, which is higher than the evaluated ferromagnetic transition temperature of 15 K. We should note that it is reasonable because the saturation magnetization includes ferromagnetic component enhanced by the applied magnetic field. The saturation magnetization (0.25 μ_B per f. u. at 2 K) is much smaller than the magnetic moment of the Co^{3+} ion (4.0 μ_B

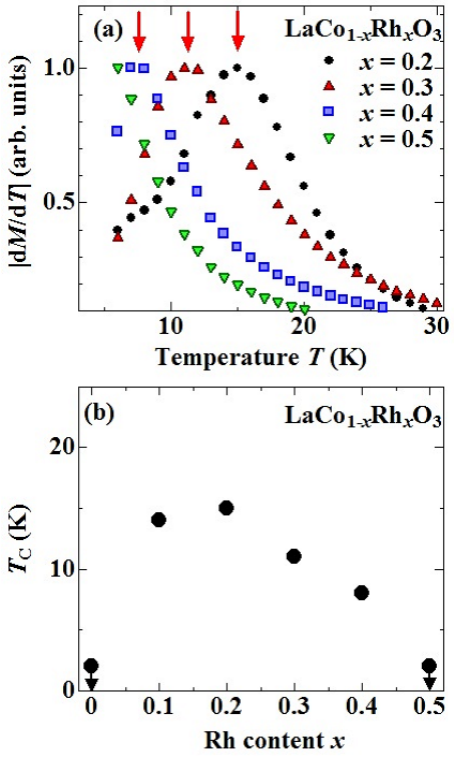

Figure 3.8: (a) Temperature dependence of $|\mathrm{d}M/\mathrm{d}T|$ of $LaCo_{1-x}Rh_xO_3$ ($0.2 \leq x \leq 0.5$) in FC process measured in 0.05 T. (b) Transition temperature for $LaCo_{1-x}Rh_xO_3$ ($0 \leq x \leq 0.5$) as a function of Rh content x.

for HS state). In contrast to M_S, $\Delta M/\Delta H$ decreases with decreasing temperature, indicating the antiferromagnetic component and/or the component which decreases with increasing ferromagnetic component.

Finally, let us discuss the time dependence of the remanent magnetization shown in Fig. 3.7(b). The remanent magnetization of $LaCo_{0.8}Rh_{0.2}O_3$ and $LaCo_{0.7}Rh_{0.3}O_3$ is different from that of $LaCo_{0.9}Rh_{0.1}O_3$, and gradually decreases with time. The data of $LaCo_{0.8}Rh_{0.2}O_3$ and $LaCo_{0.7}Rh_{0.3}O_3$ at $t > 100$ min. is well fitted by the equation given by

$$M(t)/M(t=0) = a + b\ln(t), \tag{3.1}$$

as shown by the solid lines in Fig. 3.7(b). Here we define the life time of the remanent magnetization as the time length when the magnetization decreases to a half of $M(t = 0)$. The fitting parameters a, b, and the lifetime τ of $LaCo_{0.8}Rh_{0.2}O_3$ and $LaCo_{0.7}Rh_{0.3}O_3$ are listed in Table 3.1. The lifetime τ decreases with increasing Rh content, which indicates that the Rh substitution disorder the magnetic ordering and that the system goes to the paramagnetic state.

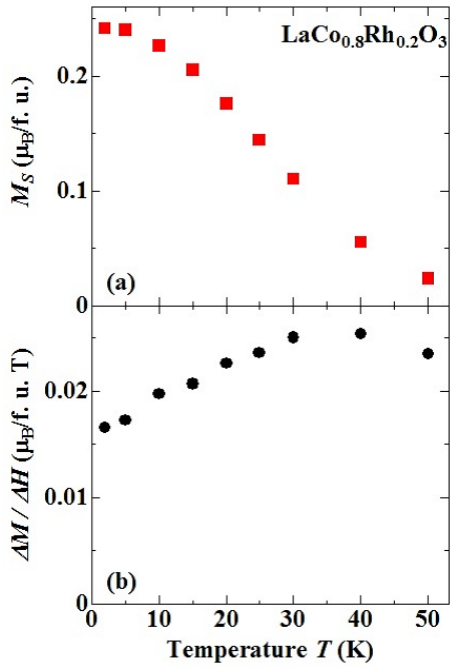

Figure 3.9: (a) Saturation magnetic moment M_S and (b) magnetic susceptibility $\Delta M/\Delta H$ of $LaCo_{0.8}Rh_{0.2}O_3$ as a function of temperature (see text).

Table 3.1: Fitting parameters a and b and the lifetime τ of $LaCo_{0.8}Rh_{0.2}O_3$ and $LaCo_{0.7}Rh_{0.3}O_3$.

Chemical formula	a	b	τ (min.)
$LaCo_{0.8}Rh_{0.2}O_3$	1.02	0.053	20700
$LaCo_{0.7}Rh_{0.3}O_3$	0.90	0.055	1470

3.3.3 Neutron scattering of $LaCo_{0.8}Rh_{0.2}O_3$

In the section 3.3.2, we discuss the complicated nature of the weak ferromagnetic ordering for $LaCo_{1-x}Rh_xO_3$. The saturation magnetization evaluated from the $M-H$ curves (0.25 μ_B per f. u. at 2 K) is much smaller than the magnetic moment of the Co^{3+} ion (4.0 μ_B for HS Co^{3+} ions), which indicates the ferromagnetic ordering with the antiferromagnetic components and/or disordering. The time-dependent remanent magnetization suggests the disordered nature of the magnetic ordering induced by the Rh substitution. Neutron scattering is a powerful probe for investigating such a complicated magnetic ordering, because the magnetic scattering owing to the ferromagnetic ordering is separated from that owing to the antiferromagnetic ordering in the reciprocal lattice space, and the width of the peak for the magnetic scattering gives

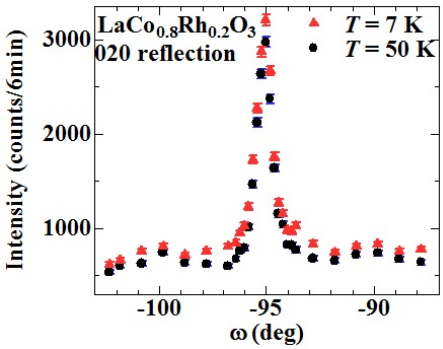

Figure 3.10: Profiles of the ω-scan (sample-angle scan) for the 020 reflection of $LaCo_{0.8}Rh_{0.2}O_3$ at 7 and 50 K.

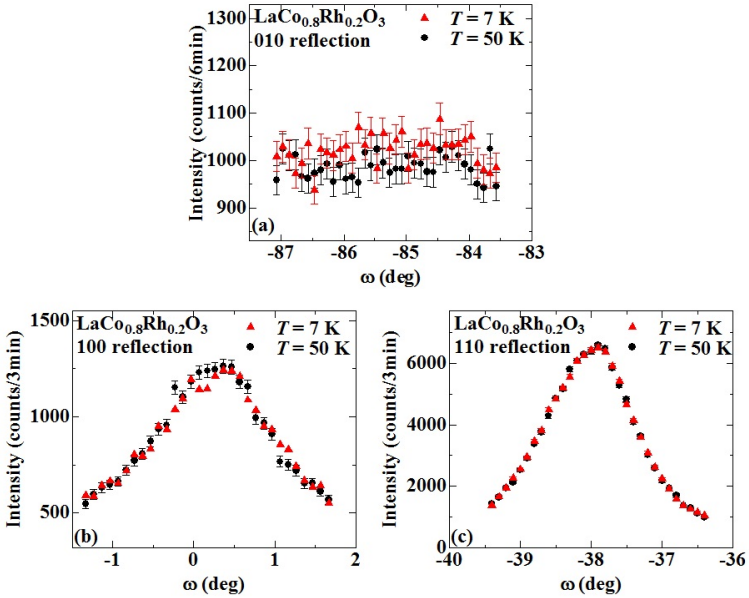

Figure 3.11: Profiles of the ω-scan for the (a) 010 reflection, (b) 100 reflection, and (c) 110 reflection of $LaCo_{0.8}Rh_{0.2}O_3$ at 7 and 50 K.

the information about a coherent length.

We first focus on the 020 reflection in order to observe the ferromagnetic ordering because the magnetic scattering is expected at the same position as the nuclear scattering when the ferromagnetic ordering emerges. Figure 3.10 shows the ω-scan (sample-angle scan) profiles for the 020 reflection of $LaCo_{0.8}Rh_{0.2}O_3$ at 7 and 50 K. The nuclear scattering is observed in the profile at 50 K. The intensity over all the ω range increases with decreasing

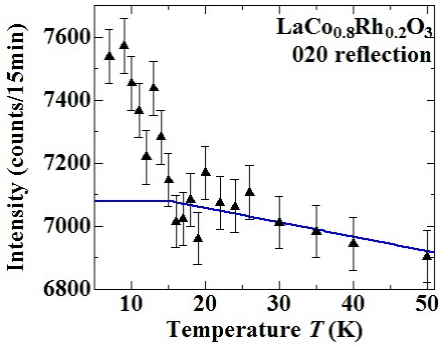

Figure 3.12: Temperature dependence of the intensity for the 020 reflection of $LaCo_{0.8}Rh_{0.2}O_3$. The solid line represents the expected temperature dependence of the magnetic diffuse scattering with the nuclear scattering (see text).

temperature, and the difference of the intensity between the profiles at 7 and 50 K is substantially larger near the nuclear scattering (ω = -95.3 deg) than at $\omega \geq$ -90 deg or $\omega \leq$ -100 deg. It indicates the contribution from the magnetic scattering for the 020 reflection at 7 K. We also focus the 010, 100, and 110 reflections of $LaCo_{0.8}Rh_{0.2}O_3$, where the magnetic scattering owing to the antiferromagnetic ordering is expected. Figure 3.11(a) shows the profile of the ω-scan for the 010 reflection of $LaCo_{0.8}Rh_{0.2}O_3$ at 7 and 50 K. The 010 reflection is not observed within the experimental error, and the background intensity is almost independent of the temperature. The profiles of the ω-scans for the 100 and 110 reflections of $LaCo_{0.8}Rh_{0.2}O_3$ at 7 and 50 K are shown in Fig. 3.11(b) and 3.11(c). The nuclear scatterings are observed, and the intensities over all the ω range does not change with temperature.

Figure 3.12 shows the temperature dependence of the intensity for the 020 reflection of $LaCo_{0.8}Rh_{0.2}O_3$, which is obtained by integrating the intensity with respect to ω from -95.3 to -94.8 deg in the ω-scan profile of $LaCo_{0.8}Rh_{0.2}O_3$. The intensity linearly increases with decreasing temperature down to 15 K, and suddenly develops below 15 K. Here let us evaluate the contribution from the magnetic scattering in the ω-scan profile of $LaCo_{0.8}Rh_{0.2}O_3$ in order to discuss the ferromagnetic ordering more quantitatively. The intensity of the 020 reflection increases down to 15 K in Fig. 3.12, possibly owing to the magnetic diffuse scattering corresponding to the increase of the magnetization down to 15 K. Here we neglect the temperature dependence of the background intensity for other contribution because there is no difference of the intensity at 7 and 50 K in the other reflections shown in Fig. 3.11(a), 3.11(b), and 3.11(c). The drastic increase of the intensity below 15 K indicates that the magnetic diffuse scattering steeply develops, or indicates that a magnetic Bragg scattering appears. We assign the increasing intensity below 15 K to the static magnetic ordering because the temperature of 15 K is identical

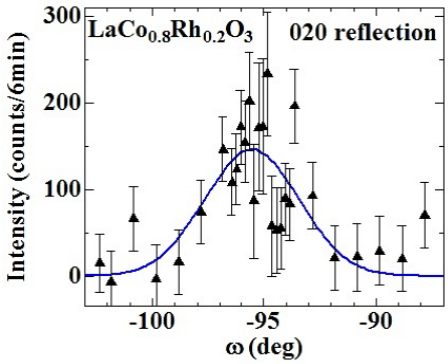

Figure 3.13: Contribution to the magnetic scattering in the ω-scan profile of $LaCo_{0.8}Rh_{0.2}O_3$ at 7 K. The solid curve represents the fitting result using a Gaussian curve (see text).

to the ferromagnetic transition temperature defined in the section 3.3.2.

Next we evaluate the contribution from the magnetic scattering below 15 K in the ω-scan profile of $LaCo_{0.8}Rh_{0.2}O_3$. Here we assume the temperature dependence of the magnetic diffuse scattering which represents in the solid line of Fig. 3.12, and roughly regard the diffuse scattering as ω-independent for -103 deg $\leq \omega \leq$ -88 deg because the diffuse scattering is expected to much broader than the nuclear one. Then, we determine the contribution from the magnetic scattering by subtracting the ω-scan profile at 50 K from that at 7 K, and correcting the background intensity. Figure 3.13 shows obtained magnetic scattering in the ω-scan profile, where the width of the magnetic scattering is larger than that of the nuclear scattering shown in Fig. 3.10. By assuming that the broad magnetic scattering arises from the ordering with a short coherent length, we can obtain the width and the integrated intensity of the ω-scan profile by fitting the experimental data to a Gaussian curve.

Let us evaluate the ordered moment of $LaCo_{0.8}Rh_{0.2}O_3$. The integrated intensity of the magnetic Bragg scattering is proportional to the squared ordered moment. In order to obtain the integrated intensity of the three dimensionally broad peak, three independent scans are necessary. Owing to experimental constraints, we only measured the ω-scan profile for the magnetic scattering. Thus we estimate contributions along two directions perpendicular to the ω-scan by considering the resolution function of our equipments. We first assume an isotropic shape with a half width of 2.5 deg for the magnetic peak because of the almost cubic symmetry of the crystal structure. Then, we have already collected the contribution from the direction perpendicular to the scattering plane in the ω-scan profile, because of a large aperture of 5 deg of our equipment in this direction, which is roughly the same width of the peak. The last direction to be considered is along the ω-2θ scan. In this direction, a number

of neutrons cannot reach the detector because of a small aperture of 0.5 deg. We roughly estimate the number to be 50 % of the total at most, judging from the counts near the peak in Fig. 3.13. Here, we can use the integrated intensity of the ω-scan profile as a lower limit of the peak intensity of the magnetic Bragg scattering,

We evaluate the ordered moment by comparing the intensity of the magnetic scattering with that of the nuclear scattering. We assume that the magnetic structure of $LaCo_{0.8}Rh_{0.2}O_3$ is a simple cubic lattice composed of Co^{3+} and Rh^{3+} ions, and find the ordered moment in Co(Rh) sites to be 0.2 $\pm$ 0.1 μ_B at least. If the uncounted neutrons is taken into account, it will be 0.4 $\pm$ 0.2 μ_B. We emphasize that it is consistent with the magnetization (0.35 μ_B per Co(Rh) site) under the applied field of 7 T at 2 K, which supports our assumption that the magnetic scattering is due to the magnetic ordering with the short coherent length. This value is much smaller than that of the HS Co^{3+} ion (4.0 μ_B). A coherent length of 26 $\pm$ 5 Å is obtained from the width of the magnetic scattering, which suggests a disordered nature of the magnetic ordering.

We finally discuss an origin of the ferromagnetic ordering of $LaCo_{1-x}Rh_xO_3$. The small ordered moment and the short coherent length imply that the magnetic ordering is the highly disordered weak ferromagnetism, which is consistent with the discussion in the section 3.3.2. We think that the substituted Rh^{3+} ions plays two role in the magnetic properties; they induce the ferromagnetic ordering by stabilizing the HS Co^{3+} ions down to lowest temperature, and suppress the ordering as the non-magnetic impurity. The small ordered moment (0.4 $\pm$ 0.2 μ_B) can be partially explained by the small HS Co^{3+} content (0.2 per Co ion). The origin of the ferromagnetic interaction between HS Co^{3+} ions is unclear because it is usually expected to be antiferromagnetic. In the strained $LaCoO_3$ thin film, the complicate spin-state ordering is important for the ferromagnetic ordering [55]. Further experiments and analysis are needed in order to discuss the ferromagnetism and the spin state of Co^{3+} in $LaCo_{1-x}Rh_xO_3$.

3.3.4 HS Co^{3+} content evaluated by the magnetization

In this section, we evaluate the HS Co^{3+} content from the magnetization. Figure 3.14 shows the temperature dependence of the reciprocal magnetic susceptibility for $LaCo_{0.8}Rh_{0.2}O_3$ taken in 1 T. The reciprocal magnetic susceptibility linearly increases with increasing temperature. Thus, we first fit the H/M - T curves from 200 to 300 K using the Curie-Weiss law as shown in Eq. 1.13, and evaluate the effective magnetic moment $\mu_{\rm eff}$ and the Curie temperature θ. The effective magnetic moment $\mu_{\rm eff}$ as a function of Rh content is shown in Fig. 3.15(a). The effective magnetic moment is close to 3 μ_B and not changed below $x = 0.5$, which indicates that the content of the magnetic HS Co^{3+} ions is almost independent of Rh content. In contrast, $\mu_{\rm eff}$ rapidly de-

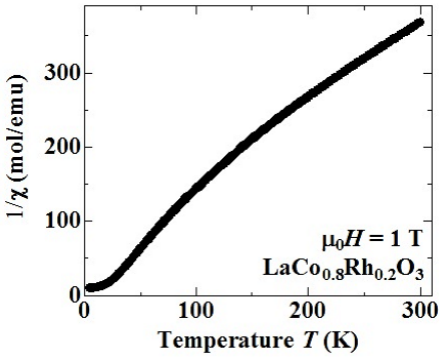

Figure 3.14: Temperature dependence of the reciprocal magnetic susceptibility for $LaCo_{0.8}Rh_{0.2}O_3$ taken in 1 T.

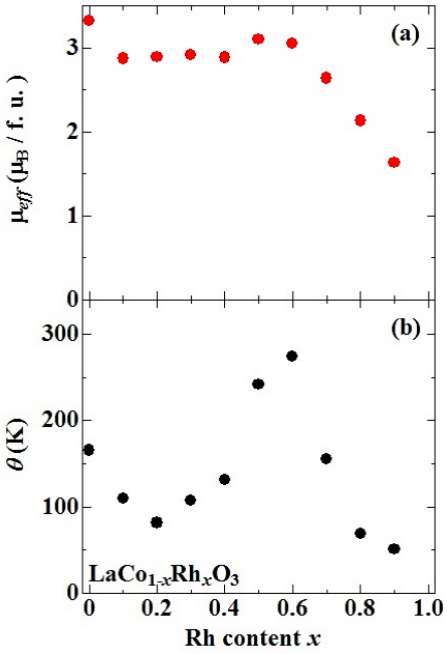

Figure 3.15: (a) Effective magnetic moment $\mu_{\rm eff}$ and (b) Weiss temperature θ as a function of Rh content.

creases with increasing Rh content for $x > 0.5$. This non-monotonic behavior of $\mu_{\rm eff}$ cannot be explained by the non-magnetic-ion substitution effect on the homogeneous system. These experimental results are roughly understood by the model that the substituted Rh^{3+} ions are preferentially substituted for LS and HS Co^{3+} ions for $x < 0.5$ and $x > 0.5$, respectively. The Weiss temperature θ as a function of Rh content is shown in 3.15(b). The positive value of θ

over all x range indicates the antiferromagnetic interaction between HS Co^{3+} ions. The Weiss temperature rapidly increases with increasing Rh content for $0.3 \leq x \leq 0.6$, and reaches 270 K at $x = 0.6$. It is not reliable because the Weiss temperature gives the antiferromagnetic transition temperature in the mean-field approximation. If the Weiss temperature for $x = 0.6$ was correctly evaluated, we could observe some magnetic transition in the magnetization for $LaCo_{0.4}Rh_{0.6}O_3$. The HS Co^{3+} content evaluated from the effective magnetic moment is about 0.4 per f. u., which is little larger than that evaluated from the lattice volume (0.25 per f. u.). These results indicate that the magnetic susceptibility of $LaCo_{1-x}Rh_xO_3$ does not simply obey the Curie-Weiss law.

Let us discuss the H/M - T curve for $LaCo_{0.8}Rh_{0.2}O_3$ shown in Fig. 3.14 in more detail. Here the Pauli paramagnetism is negligible in $LaCo_{1-x}Rh_xO_3$ because the electrical resistivity suggests that $LaCo_{1-x}Rh_xO_3$ is semiconductor below 300 K [43]. The crystal field splitting can affect the magnetization. Even if the magnetization simply obey the Curie-Weiss law at low temperature, the magnetization deviate from the Curie-Weiss law at high temperature owing to the contribution from thermally excited state when the crystal field splitting is small. Such a phenomenon can be observed in f electron systems in which the crystal field is shielded by the $5s$ and $5p$ electrons [56]. In this case, a similar H/M - T curve as shown in Fig. 3.14 may be obtained. We safely exclude this possibility because the crystal field splitting in d electron systems ($\sim 10^4$ K) is much larger than that in f electron systems. The difference between the non-magnetic-ion substitution effects shown in Chapter 4 cannot be explained when all the Co^{3+} ions have the same spin state.

Thus we assume that the magnetic moment for the magnetic ion does not change, but the content of the magnetic ion changes. In this thesis, we regard HS and LS Co^{3+} ions as two different species of ions having their unique magnetic moment, and assume the solid solution of HS Co^{3+}, LS Co^{3+}, and Rh^{3+} in Co(Rh) sites of $LaCo_{1-x}Rh_xO_3$. Thus, let us evaluate the temperature dependence of the HS Co^{3+} content by modifying the Curie-Weiss law for the spin-state crossover. When the number of the magnetic ions N in Eq. 1.13 depends on temperature ($N = N(T)$), Eq. 1.13 is rewritten as

$$\frac{\mu_0 H}{M} = \frac{3k_B}{N(T)\mu_B^2\mu_{eff}^2}T + \frac{3k_B}{N(T)\mu_B^2\mu_{eff}^2}\theta. \tag{3.2}$$

The Curie temperature θ is proportional to the number of the nearest neighbor sites of the magnetic ions z within the mean field approximation, as shown in the section 1.2.2. When the HS Co^{3+} content is changed with temperature, we can simply assume that z is proportional to $N(T)$. Since θ is proportional to $N(T)$ in this approximation, the second term of Eq. 3.2 is independent of temperature. Then we can evaluate the second term of Eq. 3.2 obtained as

$$A = \frac{3k_B}{N(T)\mu_B^2\mu_{eff}^2}\theta(T), \tag{3.3}$$

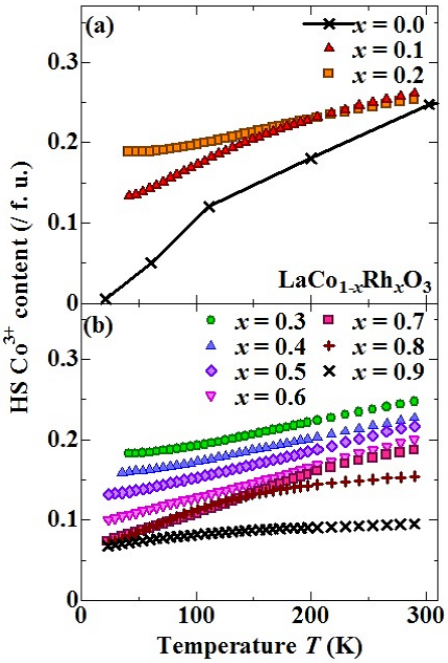

Figure 3.16: Temperature dependence of HS Co^{3+} content for $LaCo_{1-x}Rh_xO_3$ (a) ($0 \leq x \leq 0.2$) and (b) ($0.3 \leq x \leq 0.9$). $N(T)$ in $LaCoO_3$ is taken from Ref. [31].

by extrapolating the reciprocal magnetic susceptibility towards 0 K. In this study, we linearly extrapolate the reciprocal magnetic susceptibility towards 0 K for $x = 0.1$ and 0.2. The parameters A for other composition are obtained by fitting the reciprocal magnetic susceptibility to the quadratic function because of its temperature dependence. After determining the value of A, we obtain $N(T)$ from Eq. 3.2 as

$$N(T) = \frac{3k_{\mathrm{B}}T}{\mu_{\mathrm{B}}^2\mu_{\mathrm{eff}}^2(\frac{\mu_0 H}{M} - A)}. \tag{3.4}$$

Next, let us evaluate the squared effective magnetic moment of the HS Co^{3+} ion μ_{eff}^2. $g_{\parallel}$, $g_{\perp}$, and the effective spin S of the HS Co^{3+} ion are evaluated to be 3.35, 3.55, and 1 from ESR, respectively [20], which indicates that spin-orbit interaction is not negligible. We can roughly evaluate μ_{eff}^2 to be about 24 by ignoring the anisotropy of g factor. The evaluated value is the same as that of the orbital-quenched HS Co^{3+} ion (g = 2, S = 2, $\mu_{\mathrm{eff}}^2 = 24$). In other words, from the Curie-Weiss susceptibility J = 1(S = 2, L = 1) and S = 2 (L = 0) give roughly the same μ_{eff}^2. Here we set $\mu_{\mathrm{eff}}^2 = 24$ as the HS state value.

Figure 3.16(a) and 3.16(b) show the temperature dependence of HS Co^{3+} content for $LaCo_{1-x}Rh_xO_3$ ($0 \leq x \leq 0.2$) and ($0.3 \leq x \leq 0.9$), respectively.

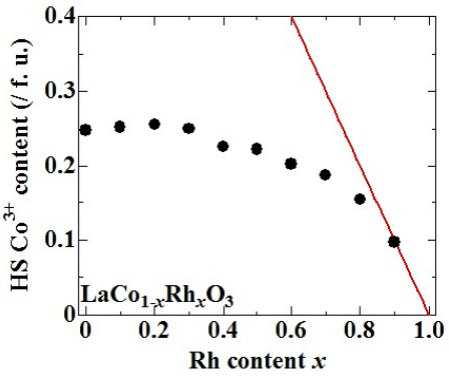

Figure 3.17: HS Co^{3+} content at 300 K as a function of Rh content. $N(T)$ in $LaCoO_3$ is taken from Ref. [31]. The solid line represents the content of Co^{3+} ions expected from the chemical formula.

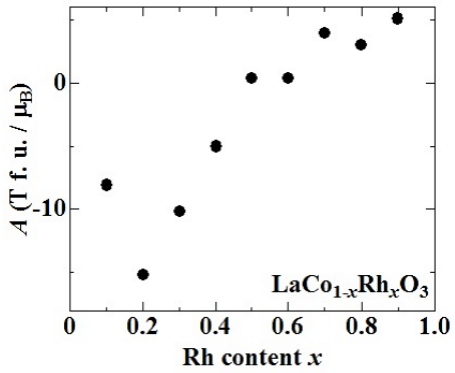

Figure 3.18: Rh content dependence of the parameter A for $LaCo_{1-x}Rh_xO_3$.

With decreasing temperature, $N(T)$ of $LaCoO_3$ decreases to zero at low temperature. In contrast, $N(T)$ for Rh substituted samples decreases with decreasing temperature and have a finite value at 40 K, which indicates that the Rh^{3+} substitution stabilizes the HS Co^{3+} down to low temperatures. Note that $N(300\ \mathrm{K})$ of 0.25 per f. u. are almost the same value for $0 \leq x \leq 0.3$, which indicates that the Rh^{3+} substitution does not change the HS Co^{3+} content. We emphasize that the HS Co^{3+} content evaluated from the magnetization shown in Fig. 3.16(a) is quantitatively consistent with that evaluated from the lattice volume shown in Fig. 2.8. The HS Co^{3+} content gradually decreases with increasing Rh content for $x > 0.3$ below 300 K, and finally independent of temperature at $x = 0.9$, where all the Co^{3+} ions take the HS state. Figure 3.17 shows the HS Co^{3+} content at 300 K as a function of Rh content, which has the similar Rh content dependence with the effective magnetic moment shown

in Fig. 3.15. The HS Co^{3+} content approach to the Co^{3+} content expected from the chemical formula, which is represented by the solid line. We should note that this analysis based on the IS model is obviously wrong. If the IS model were valid, we would set $\mu_{\rm eff}^2 = 8$ as the IS state value in Eq. 3.4. Then, the evaluated $N(T)$ is three times larger than that of HS Co^{3+} ions, which is larger than the Co^{3+} content for $x \geq 0.3$. The HS-LS model are reasonable to explain the magnetization of $LaCo_{1-x}Rh_xO_3$. Rh content dependence of the parameter A for $LaCo_{1-x}Rh_xO_3$ is shown in Fig. 3.18. The negative values are obtained for $0.1 \leq x \leq 0.4$, meaning that the interaction between the HS Co^{3+} ions are ferromagnetic. The value takes a minimum at $x = 0.2$, and increases with increasing Rh content. The small positive values are obtained for $x \geq 0.5$. The change of A with Rh substitution is strange because the parameter A is not changed by the substitution in the mean field approximation. It may be due to that the magnetic interaction between the HS Co^{3+} ions are more sensitive to the HS Co^{3+} content than that expected from the mean field approximation, possibly owing to the small HS Co^{3+} content.

3.4 Summary

We have carried out the magnetization measurements of the polycrystalline samples for $LaCo_{1-x}Rh_xO_3$ and the neutron scattering for a single crystal of $LaCo_{0.8}Rh_{0.2}O_3$. We have found the hysteresis between the magnetization in ZFC and FC process for $0.1 \leq x \leq 0.4$ and the spontaneous magnetization in $M-H$ curve for $LaCo_{0.8}Rh_{0.2}O_3$ at 2 K. The magnetization does not saturate and linearly increases with increasing applied magnetic field, and the value at 7 T (0.35 $\mu_{\rm B}$ per f. u. at 2 K) is much smaller than the magnetic moment of the Co^{3+} ion (4.0 $\mu_{\rm B}$ for HS state), which indicates the weak ferromagnetic ordering. Corresponding to the magnetic ordering, the neutron scattering intensity of the 020 reflection for $LaCo_{0.8}Rh_{0.2}O_3$ sharply increases with decreasing temperature below 15 K, and the magnetic scattering is observed in the ω-scan profile at 7 K. We evaluate the ordered moment in Co(Rh) sites to be 0.4 ± 0.2 $\mu_{\rm B}$, which is consistent with the magnetization of $LaCo_{0.8}Rh_{0.2}O_3$. The evaluated coherent length is 26 ± 5 Å, which indicates that the ferromagnetic ordering of $LaCo_{0.8}Rh_{0.2}O_3$ originates from the short-range ferromagnetic ordering disordered by Rh^{3+} ions. We evaluate the HS Co^{3+} content of $LaCo_{1-x}Rh_xO_3$ from the magnetization by using the modified Curie-Weiss law. The evaluated HS Co^{3+} contents as a function of temperature and Rh content are consistent with that evaluated from the lattice volume shown in the section 2.3.3. In contrast to that of $LaCoO_3$, the HS Co^{3+} content of the Rh substituted samples have a finite value at the lowest temperature. The HS Co^{3+} content is independent of the Rh content for $0 \leq x \leq 0.5$ at room temperature and gradually decreases down to 0 with increasing Rh content for $0.5 \leq x \leq 0.9$, which indicates that the Rh^{3+} ions preferentially reduce

the LS Co^{3+} ions. This analysis cannot be applied to the IS model because the evaluated IS Co^{3+} content is larger than the maximum expected from the chemical formula for $x > 0.3$. It supports the HS-LS model as the spin state of Co^{3+} ions in $LaCo_{1-x}Rh_xO_3$.

Chapter 4

Ga substitution effects on the spin state of Co^{3+} ions in $LaCo_{0.8}Rh_{0.2}O_3$

4.1 Introduction

In this chapter, we show the Ga substitution effects for $LaCo_{0.8}Rh_{0.2}O_3$ on the structural and magnetic properties. In Chapters 2 and 3, we discuss the spin state of Co^{3+} ions and its crossover phenomena for $LaCo_{1-x}Rh_xO_3$ through the structural and magnetic properties. These experimental results support the HS-LS model as the spin state of Co^{3+} ions for $LaCo_{1-x}Rh_xO_3$, and indicate that the Rh substitution suppresses the spin-state crossover and stabilizes the HS Co^{3+} ions at lowest temperature. The evaluated HS Co^{3+} content for $LaCo_{1-x}Rh_xO_3$ is almost independent of Rh content for $0 \leq x \leq 0.5$ at room temperature, and gradually decreases down to 0 with increasing Rh content for $0.5 \leq x \leq 0.9$. The Rh substitution effects cannot be explained by the simple dilution effects. According to the Kyomen's idea shown in the section 1.4, we can expect that the substituted Ga^{3+} ions behave as the HS Co^{3+} ions and stabilize the LS Co^{3+} ions. We have measured the x-ray diffraction and the magnetization of $LaCo_{0.8-y}Rh_{0.2}Ga_yO_3$ ($0 \leq y \leq 0.15$), in order to discuss the difference between the non-magnetic-ion substitution effects on the spin state of Co^{3+} ions. We choose the Rh substituted sample as the initial phase for the Ga substitution instead of $LaCoO_3$ because the Rh substitution suppress the spin-state crossover, which enable us to discuss the magnetization of the Ga substituted samples by using the modified Curie-Weiss law as shown in the section 3.3.4. We select the composition with the highest ferromagnetic transition temperature in order to discuss the Ga substitution effects on the ferromagnetic ordering. We finally evaluate the HS Co^{3+} content of $LaCo_{0.8-y}Rh_{0.2}Ga_yO_3$, and discuss the origin of the non-magnetic-ion substitution effects.

4.2 Experiment

Polycrystalline samples of $LaCo_{0.8-y}Rh_{0.2}Ga_yO_3$ ($0 \leq y \leq 0.15$) were prepared by a solid-state reaction, which is similar to that shown in the section 2.2. A mixture of La_2O_3 ($3N$), Co_3O_4 ($3N$), Rh_2O_3 ($3N$), and Ga_2O_3 ($4N$) with stoichiometric molar ratios was ground and calcined for 24 hour at 1000 °C in air. The calcined powder was ground, pressed into a pellet, and sintered for 48 hour at 1200 °C in air. These pellets were cooled slowly down to room temperature in the furnace by switching off the power after sintering. X-ray diffraction was measured with a Rigaku RAD-IIC (Cu Kα radiation), and no impurity phases were detected for the prepared samples. Magnetization in field cooling (FC) and zero field cooling (ZFC) processes were measured using a SQUID magnetometer (Quantum Design MPMS) from 5 to 300 K in an applied field of 0.05 and 1 T for $LaCo_{0.8-y}Rh_{0.2}Ga_yO_3$ ($0 \leq y \leq 0.15$). Magnetization-field (M - H) curves at $T = 2$ K for $LaCo_{0.8-y}Rh_{0.2}Ga_yO_3$ ($0 \leq y \leq 0.15$) were measured in sweeping $\mu_0 H$ from 0 to 7 T, and from 7 to 0 T.

4.3 Results and Discussion

4.3.1 Structural and magnetic properties of $LaCo_{0.8-y}Rh_{0.2}Ga_yO_3$

The CuKα x-ray diffraction patterns of $LaCo_{0.8-y}Rh_{0.2}Ga_yO_3$ ($0 \leq y \leq 0.15$) are similar to that of $LaCo_{0.8}Rh_{0.2}O_3$, which indicates that the crystal system of the samples at room temperature remains orthorhombic. Figure 4.1 shows the lattice parameters for $LaCo_{0.8-y}Rh_{0.2}Ga_yO_3$ ($0 \leq y \leq 0.15$). All the lattice parameters are essentially independent of Ga content. The lattice volume of $LaCo_{0.8-y}Rh_{0.2}Ga_yO_3$ as a function of Ga content is shown in Fig. 4.2. For comparison, the lattice volume of $LaCo_{1-x}Rh_xO_3$ ($0.2 \leq x \leq 0.4$)

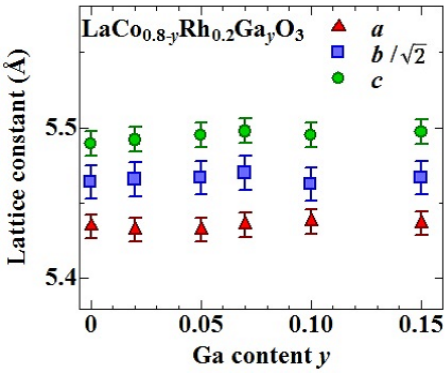

Figure 4.1: Lattice parameters of $LaCo_{0.8-y}Rh_{0.2}Ga_yO_3$ as a function of Ga content.

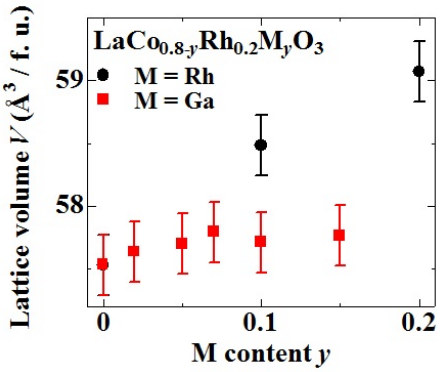

Figure 4.2: Lattice volume of $LaCo_{0.8-y}Rh_{0.2}M_yO_3$ (M=Rh, Ga) as a function of M content.

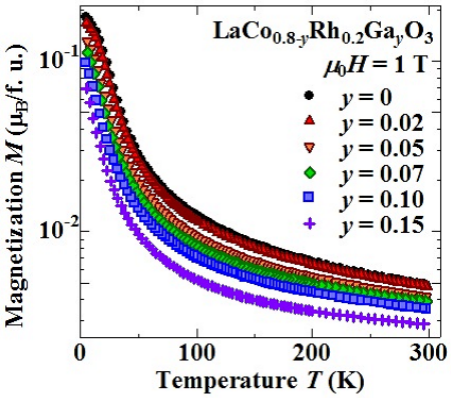

Figure 4.3: Temperature dependence of the magnetization for $LaCo_{0.8-y}Rh_{0.2}Ga_yO_3$ ($0 \leq y \leq 0.15$) taken in 1 T.

is also plotted. The lattice volume of $LaCo_{0.8-y}Rh_{0.2}Ga_yO_3$ is independent of Ga content, which remarkably differs from the Rh substitution effect. Because the ionic radius of the Ga ion (0.62 Å) is substantially larger than that of the LS Co^{3+} ion (0.545 Å), and is close to that HS Co^{3+} ion (0.61 Å), these experimental results suggest that the Ga^{3+} ions behave as if they were preferentially substituted for the HS Co^{3+} ions.

Figure 4.3 shows the temperature dependence of the magnetization for $LaCo_{0.8-y}Rh_{0.2}Ga_yO_3$ per f. u. in the range of $0 \leq y \leq 0.15$ taken in 1 T. The magnetization of $LaCo_{0.8}Rh_{0.2}O_3$ shows the Curie-Weiss-like behavior below room temperature. The magnetization in all the temperature range decreases with increasing Ga content, whereas the Curie-Weiss-like temperature dependence remains. Figure 4.4 shows the temperature dependence of mag-

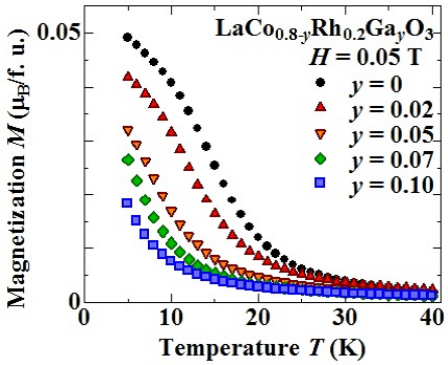

Figure 4.4: Temperature dependence of the magnetization in the FC process for $LaCo_{0.8-y}Rh_{0.2}Ga_yO_3$ ($0 \leq y \leq 0.15$) taken in 0.05 T.

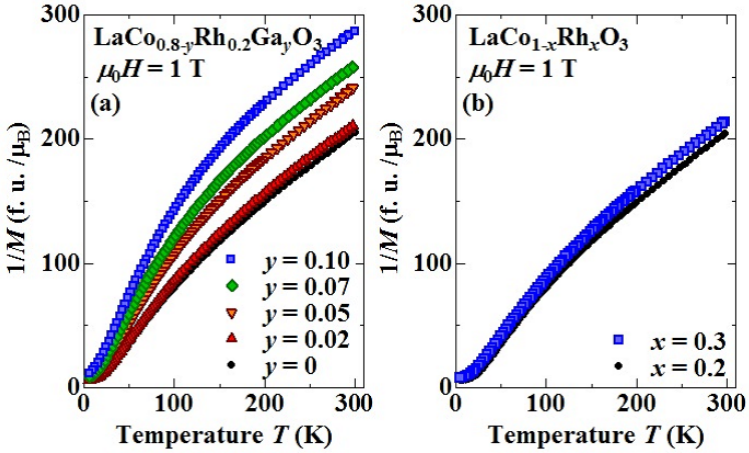

Figure 4.5: Temperature dependence of the reciprocal magnetization for (a) $LaCo_{0.8-y}Rh_{0.2}Ga_yO_3$ ($0 \leq y \leq 0.1$) and (b) $LaCo_{1-x}Rh_xO_3$ (x = 0.2 and 0.3).

netization in the FC process for $LaCo_{0.8-y}Rh_{0.2}Ga_yO_3$ ($0 \leq y \leq 0.15$) taken in 0.05 T. The inflection point of the $M - T$ curve is observed at $T_C = 15$ K for $LaCo_{0.8}Rh_{0.2}O_3$. Transition temperature shifts down to low temperature with increasing Ga content, and disappears for $y \geq 0.07$.

Figure 4.5(a) and 4.5(b) show the temperature dependence of the reciprocal magnetization for $LaCo_{0.8-y}Rh_{0.2}Ga_yO_3$ ($0 \leq y \leq 0.1$) and $LaCo_{1-x}Rh_xO_3$ ($x = 0.2$ and 0.3), respectively. The inverse magnetization of $LaCo_{0.8}Rh_{0.2}O_3$ drastically increases by the 10% Ga substitution, whereas it is not changed by the 10% Rh substitution. We should note that the inverse magnetization of Ga substituted samples linearly increases with increasing temperature above 200 K. In terms of the conventional Curie-Weiss law, it gives the results that the

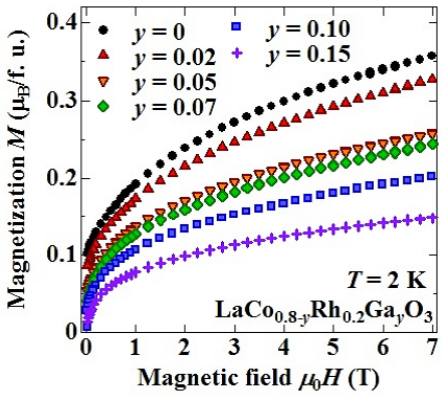

Figure 4.6: Magnetization-field curve in the H-decreasing process for $LaCo_{0.8-y}Rh_{0.2}Ga_yO_3$ ($0 \leq y \leq 0.15$) taken at 2 K.

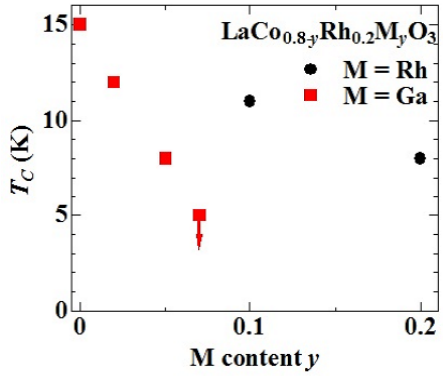

Figure 4.7: Transition temperature for $LaCo_{0.8-y}Rh_{0.2}M_yO_3$ (M=Rh, Ga) as a function of M content.

Weiss temperature increases with increasing Ga content, which is not probable for the non-magnetic-ion substitution effects. It means that the change of the HS Co^{3+} content with temperature should be considered.

Figure 4.6 shows the M - H curve in the H-decreasing process at $T = 2$ K for $LaCo_{0.8-y}Rh_{0.2}Ga_yO_3$ ($0 \leq y \leq 0.15$). The spontaneous magnetization observed for $y = 0$ is strongly suppressed by Ga substitution, and is not visible for $y \geq 0.10$. These experimental results suggest that the weak ferromagnetism is suppressed by Ga substitution.

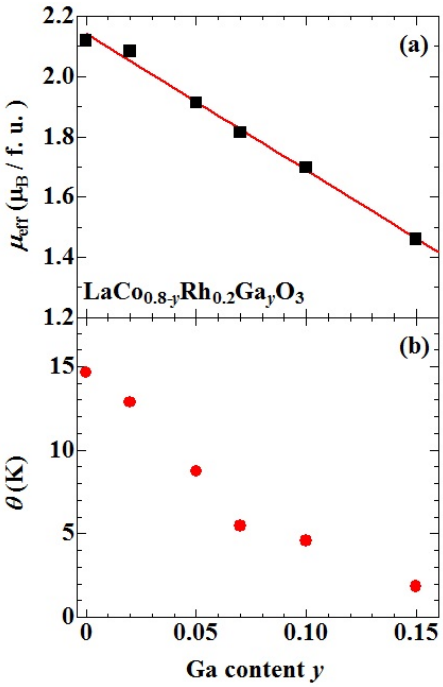

Figure 4.8: Ga content dependence of (a) the effective magnetic moment and (b) the Weiss temperature for $LaCo_{0.8-y}Rh_{0.2}Ga_yO_3$ ($0 \leq y \leq 0.15$) which are evaluated from fitting the *H/M* - *T* curves for $LaCo_{0.8-y}Rh_{0.2}Ga_yO_3$ ($0 \leq y \leq 0.15$) from 40 to 70 K using the Curie-Weiss law. The solid line in (a) represents the linear fit to the data.

4.3.2 Magnetic dilution effect

In this section, we further discuss the Ga substitution effects on the magnetic properties for $LaCo_{0.8}Rh_{0.2}O_3$. Figure 4.7 shows the Ga content dependence of the transition temperature for $LaCo_{0.8-y}Rh_{0.2}M_yO_3$ (M=Rh, Ga) defined by the same way shown in the section 3.3.2. The transition temperature linearly decreases with increasing Ga content, and finally cannot be observed at $y = 0.07$. It should be noted that we can define T_C above 5 K up to $y = 0.2$ for M = Rh, which indicates that the Ga substitution suppress the weak ferromagnetism more than Rh substitution.

As shown in Fig. 3.16, the HS Co^{3+} content of $LaCo_{0.8}Rh_{0.2}O_3$ is almost independent of temperature below 70 K. We thus can evaluate the HS Co^{3+} content below 70 K from the magnetization by using the conventional Curie-Weiss law. Figure 4.8(a) shows the Ga content dependence of μ_{eff} for $LaCo_{0.8-y}Rh_{0.2}Ga_yO_3$ ($0 \leq y \leq 0.15$), which are evaluated from fitting the H/M - T curves from 40 to 70 K using the Curie-Weiss law. The evaluated μ_{eff} is 2.1 μ_B for $y = 0$, which linearly decreases with increasing Ga content.

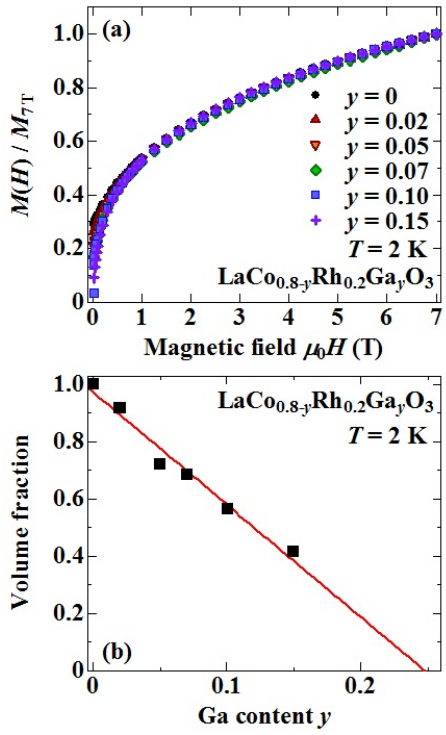

Figure 4.9: (a)Magnetization - field curves normalized by the value of the magnetization taken in 7 T for $LaCo_{0.8-y}Rh_{0.2}Ga_yO_3$ ($0 \leq y \leq 0.15$) at 2 K. (b) Ga content dependence of the volume fraction (see text) for $LaCo_{0.8-y}Rh_{0.2}Ga_yO_3$ ($0 \leq y \leq 0.15$) at 2 K. The solid line represents the linear fit of the data.

We evaluate from the slope of the solid line shown in Fig. 4.8(a) that one Ga^{3+} ion decreases the effective magnetic moment of 4.6 μ_B, which is similar value to that of the HS Co^{3+} of 4.9 μ_B. In the simplest approximation, it indicates that the Ga^{3+} ions behave as if they were preferentially substituted for the HS Co^{3+} ions. The Ga content dependence of θ is shown in Fig. 4.8(b), where θ linearly decreases with increasing Ga content. This indicates that the magnetic interaction between the HS Co^{3+} ions is suppressed by Ga substitution, which is consistent with the experimental results suggesting that the Ga^{3+} ions rapidly reduce the HS Co^{3+} ions.

Figure 4.9(a) shows M - H curves normalized by the value of magnetization at $\mu_0 H = 7$ T for $LaCo_{0.8-y}Rh_{0.2}Ga_yO_3$ ($0 \leq y \leq 0.15$), where all the curves fall onto a single curve above 3 T. It shows that the Ga substitution dilutes the magnetization of $LaCo_{0.8}Rh_{0.2}O_3$. The normalization factor is shown in Fig. 4.9(b), which can be regarded as the volume fraction of the magnetic phase in a simplest approximation. The volume fraction linearly decreases with increasing Ga content, indicating that the HS Co^{3+} ions are

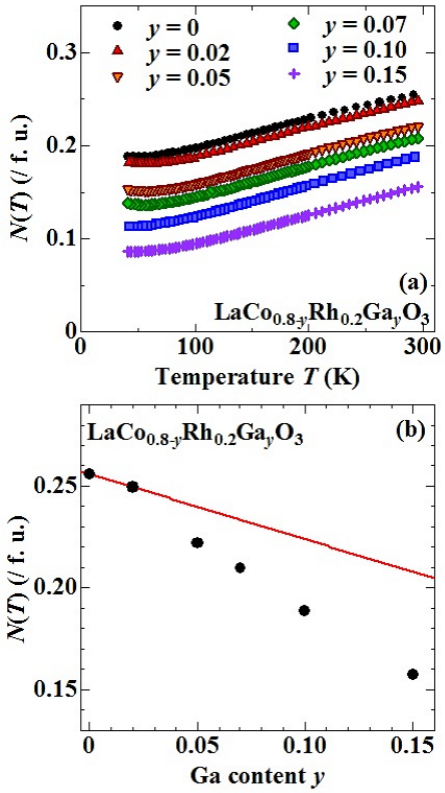

Figure 4.10: (a) The content of the high-spin state Co^{3+} in $LaCo_{0.8-y}Rh_{0.2}Ga_yO_3$ ($0 \leq y \leq 0.15$) plotted as a function of temperature. (b) HS Co^{3+} content at 300 K as a function of Ga content. The solid line represents the HS Co^{3+} content expected from the dilution effect.

reduced by Ga substitution. We evaluate from the solid line shown in Fig. 4.9(b) the critical concentration to be $y = 0.25$ at which the magnetic volume fraction disappears. It should be emphasized that the critical value of 0.25 is almost the same with the HS Co^{3+} content of $LaCo_{0.8}Rh_{0.2}O_3$ at lowest temperature (0.2 per f. u.). This reinforce the indication that the Ga^{3+} ions behave as if they were preferentially substituted for the HS Co^{3+} ions. We should emphasize that the Ga substitution effects cannot be explained in the system where the Co^{3+} ions can take only one spin state. If all the Co^{3+} ions had one spin state, the lattice volume and magnetization could be determined corresponding to the spin state. In this case, the obtained Ga content dependence of the lattice volume suggests that the spin state of Co^{3+} ions is not changed by the Ga^{3+} substitution. Then, the Ga substitution decreases the magnetization by decreasing the Co^{3+} content. Experimental results show that the Ga substitution more strongly decreases the magnetization.

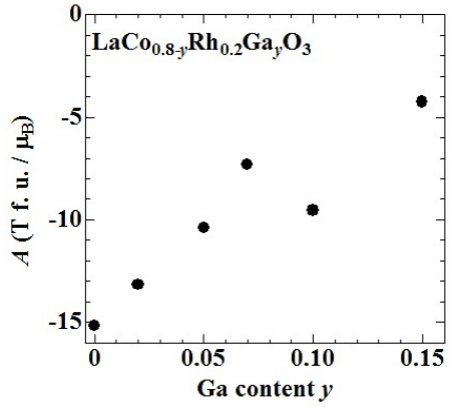

Figure 4.11: Ga content dependence of the parameter A for $LaCo_{0.8-y}Rh_{0.2}Ga_yO_3$ ($0 \leq y \leq 0.15$) (see text).

Finally, we evaluate the HS Co^{3+} content for $LaCo_{0.8-y}Rh_{0.2}Ga_yO_3$ from the magnetization by using the modified Curie-Weiss law shown in the section 3.3.4. Figure 4.10(a) shows the HS Co^{3+} content $N(T)$ in $LaCo_{0.8-y}Rh_{0.2}Ga_yO_3$ ($0 \leq y \leq 0.15$). $N(T)$ of $LaCo_{0.8-y}Rh_{0.2}Ga_yO_3$ ($0 \leq y \leq 0.15$) exhibits a downward parallel shift, which suggests that the Ga substitution effects are static and local. The HS Co^{3+} content at 300 K as a function of Ga content is shown in Fig. 4.10(b). $N(T)$ linearly decreases with increasing Ga content, and the slope is larger than that expected from the dilution effect shown by the solid line in Fig 4.10(b), which is consistent with the experimental results shown above. Figure 4.11 shows the Ga content dependence of the constant A, which linearly decreases with increasing Ga content.

4.3.3 Discussion on the non-magnetic-ion substitution effects

In this section, we discuss the origin of the non-magnetic-ion substitution effects. We assume the solid solution of the HS Co^{3+}, LS Co^{3+}, Rh^{3+}, and Ga^{3+} ions in Rh and Ga substituted samples. We have found that the substituted Ga^{3+} ions behave as if they were preferentially substituted for the HS Co^{3+} ions, which is different from the Rh substitution effects. At room temperature, the HS Co^{3+} is not changed with Rh substitution, which indicates that the substituted Rh^{3+} ions behave as if they were preferentially substituted for the LS Co^{3+} ions. These behaviors strongly supports the HS-LS model as the spin state of Co^{3+} ions. In contrast, the HS Co^{3+} content of Rh substituted samples shown in Fig. 3.17 has a finite value at low temperature. It indicates that the Rh substitution suppresses the spin-state crossover of Co^{3+} ions in $LaCoO_3$ and keeps HS Co^{3+} down to the lowest temperature. Similary, we can also expect that the substituted Ga^{3+} ions stabilize the LS Co^{3+} ions or accelerate

the spin-state crossover from higher temperature. The spin-state crossover around 100 K in $LaCoO_3$ is unique in the perovskite oxides $Ln CoO_3$ (Ln=La, Y, rare-earth) [57], whereas the metal-insulator transition around 500 K is observed in all the perovskite oxides $RCoO_3$ (R=trivalent rare-earh) [58]. We should consider the non-magnetic-ion substitution effects on the dynamical lattice distortion of $LaCoO_3$ in order to understand the origin of the temperature dependence of the HS Co^{3+} content. Further investigation and analysis for the dynamical distortion should be conducted, which is in progress.

4.4 Summary

We have measured the magnetization and the lattice volume for the polycrystalline samples of $LaCo_{0.8-y}Rh_{0.2}Ga_yO_3$ ($0 \leq y \leq 0.15$). The magnetization decreases by Ga substitution more strongly than by Rh substitution, and the lattice volume is almost independent of Ga substitution. These results suggest that a Ga^{3+} ion behaves as if it were selectively substituted for a HS Co^{3+} ion. We find that a Ga^{3+} ion reduce an effective magnetic moment of 4.6 μ_B, which is close to the effective magnetic moment (4.9 μ_B) of high-spin state Co^{3+}. We further find that critical concentration of 25 % at which all the HS Co^{3+} ions are substituted for Ga $^{3+}$ ions from the $M-H$ curves at 2 K, which reinforce the suggestion of the selective Ga substitution effects. We evaluate the temperature dependence of the HS Co^{3+} content in $LaCo_{0.8-y}Rh_{0.2}Ga_yO_3$ ($0 \leq y \leq 0.15$), and find that the Ga substitution effects are local and static. We conclude that Ga^{3+} and Rh^{3+} ions behave as if they were preferentially substituted for HS Co^{3+} and LS Co^{3+} ions, respectively. These results strongly support that there are HS and LS Co^{3+} ions in $LaCoO_3$ at room temperature.

Chapter 5

Conclusion

The perovskite type oxide $LaCoO_3$ has been extensively investigated as the spin-state crossover oxide. $LaCoO_3$ is non-magnetic at the lowest temperature, and the magnetization steeply increases with increasing temperature at around 30 K accompanied with the anomalous lattice expansion owing to the spin-state crossover. The spin state of magnetic Co^{3+} ions taking the high-spin or intermediate-spin state is controversial until now. The non-trivial substitution effects on the magnetization are observed for this material in this study, which cannot be explained by the magnetic dilution and chemical pressure effects. In particular, 4 % Rh substitution substantially suppresses the spin-state crossover, and Curie-Weiss-like magnetization is stabilized down to the lowest temperature. In order to discuss the spin state of Co^{3+} ions in $LaCoO_3$ through the non-magnetic-ion substitution effects, we investigated the structural and magnetic properties of $LaCo_{1-x}Rh_xO_3$ and $LaCo_{0.8-y}Rh_{0.2}Ga_yO_3$. In this analysis, we regard the different spin state of Co^{3+} ions as the different ions having their unique ionic radii and the magnetic moment, and assume the solid solution of the Co^{3+}, Rh^{3+}, and Ga^{3+} ions in these samples.

In order to investigate the spin state of Co^{3+} ions and its crossover phenomena in Rh substituted samples, we first carried out the CuKα x-ray diffraction for polycrystalline samples of $LaCo_{1-x}Rh_xO_3$ for $0 \leq x \leq 0.9$, synchrotron powder x-ray diffraction for $LaCo_{0.9}Rh_{0.1}O_3$ and $LaCo_{0.8}Rh_{0.2}O_3$, and neutron powder diffraction for $LaCo_{0.8}Rh_{0.2}O_3$. The regular CoO_6 octahedra of $LaCo_{0.8}Rh_{0.2}O_3$ determined by the neutron diffraction suggests that there are high-spin and low-spin state Co^{3+} ions in $LaCo_{0.8}Rh_{0.2}O_3$. The lattice volume of $LaCo_{0.9}Rh_{0.1}O_3$ and $LaCo_{0.8}Rh_{0.2}O_3$ as a function of temperature ceases to decrease around 70 K on cooling, which indicates that the Rh substitution suppress the spin-state crossover. We evaluate the high-spin-state Co^{3+} content for $LaCo_{1-x}Rh_xO_3$ as a function of temperature and Rh content. At room temperature, the HS Co^{3+} content is almost independent of Rh content, which indicates that Rh substitution does not change the high-spin-state Co^{3+} content.

We next measured the magnetization of the polycrystalline samples for $LaCo_{1-x}Rh_xO_3$ and the neutron scattering for a single crystal of $LaCo_{0.8}Rh_{0.2}O_3$ in order to discuss the Rh substitution effects more quantitatively. We have found the hysteresis between the magnetization in ZFC and FC process for $0.1 \leq x \leq 0.4$, which indicates the ferromagnetic ordering. The spontaneous magnetization in $M - H$ curve is observed for $LaCo_{0.8}Rh_{0.2}O_3$ at 2 K. The small saturation magnetic moment (0.25 μ_B per f. u. at 2 K) is much smaller than the magnetic moment of the Co^{3+} ion (4.0 μ_B for the high-spin state), which is consistent with the ordered moment obtained from the neutron scattering measurements (0.4 $\pm$ 0.2 μ_B). The coherent length evaluated from the width of the magnetic scattering is 26 $\pm$ 5 Å, which indicates that the ferromagnetic ordering of $LaCo_{0.8}Rh_{0.2}O_3$ originates from the short-range ferromagnetic ordering disordered by Rh^{3+} ions. We evaluate the Rh content and temperature dependence of the high-spin-state Co^{3+} content for $LaCo_{1-x}Rh_xO_3$ from the magnetization by using the modified Curie-Weiss law, which is quantitatively consistent with that evaluated from the lattice volume. These experimental results indicate that the Rh^{3+} ions behave as if they were preferentially substituted for the low-spin-state Co^{3+} ions at room temperature, and stabilize the high-spin-state Co^{3+} ions down to the lowest temperature to induce the ferromagnetic ordering.

Finally, we have measured the magnetization and the lattice volume for the polycrystalline samples of $LaCo_{0.8-y}Rh_{0.2}Ga_yO_3$ ($0 \leq y \leq 0.15$) in order to discuss the difference between the non-magnetic-ion substitution effects on the spin state of Co^{3+} ions. Ga substitution strongly reduce the magnetization, and the lattice volume is almost independent of Ga substitution. It suggest that a substituted Ga^{3+} ion behaves as if it were selectively substituted for a high-spin-state Co^{3+} ion. These results cannot be explained if all the Co ions have the identical spin state, which strongly supports that there are high-spin and low-spin states in $LaCoO_3$ at room temperature.

References

[1] Y. Tanabe and S. Sugano: J. Phys. Soc. Jpn. **9** (1954) 753.

[2] Y. Tanabe and S. Sugano: J. Phys. Soc. Jpn. **9** (1954) 766.

[3] W. A. Baker and H. M. Bobonich: Inorg. Chem. **3** (1964) 1184.

[4] E. Koenig and K. Madeja: Inorg. Chem. **6** (1967) 48.

[5] M. Sorai and S. Seki: J. Phys. Soc. Jpn. **32** (1972) 575.

[6] R. Heikes, R. Miller, and R. Mazelsky: Physica **30** (1964) 1600.

[7] K. Asai, P. Gehring, H. Chou, and G. Shirane: Phys. Rev. B **40** (1989) 10982.

[8] K. Sato, A. Matsuo, K. Kindo, Y. Kobayashi, and K. Asai: J. Phys. Soc. Jpn. **78** (2009) 093702.

[9] T. Vogt, J. A. Hriljac, N. C. Hyatt, and P. Woodward: Phys. Rev. B **67** (2003) 140401.

[10] T. Nakamura, T. Shimura, M. Itoh, and Y. Takeda: J. Solid State Chem. **103** (1993) 523 .

[11] T. Kyômen, Y. Asaka, and M. Itoh: Phys. Rev. B **67** (2003) 144424.

[12] K. Asai, A. Yoneda, O. Yokokura, J. M. Tranquada, G. Shirane, and K. Kohn: J. Phys. Soc. Jpn. **67** (1998) 290.

[13] H. Inaba and H. Tagawa: J. Ceram. Soc. Jpn. **106** (1998) 272.

[14] P. G. Radaelli and S.-W. Cheong: Phys. Rev. B **66** (2002) 094408.

[15] D. Louca, J. L. Sarrao, J. D. Thompson, H. Röder, and G. H. Kwei: Phys. Rev. B **60** (1999) 10378.

[16] S. Yamaguchi, Y. Okimoto, and Y. Tokura: Phys. Rev. B **55** (1997) R8666.

[17] A. Ishikawa, J. Nohara, and S. Sugai: Phys. Rev. Lett. **93** (2004) 136401.

[18] K. Berggold, M. Kriener, C. Zobel, A. Reichl, M. Reuther, R. Müller, A. Freimuth, and T. Lorenz: Phys. Rev. B **72** (2005) 155116.

[19] S. R. Giblin, I. Terry, D. Prabhakaran, A. T. Boothroyd, and C. Leighton: Phys. Rev. B **79** (2009) 174410.

[20] S. Noguchi, S. Kawamata, K. Okuda, H. Nojiri, and M. Motokawa: Phys. Rev. B **66** (2002) 094404.

[21] M. Itoh, M. Sugahara, I. Natori, and K. Motoya: J. Phys. Soc. Jpn. **64** (1995) 3967.

[22] M. Senaris-Rodriguez and J. Goodenough: J. Solid State Chem. **116** (1995) 224.

[23] Y. Tokura, Y. Okimoto, S. Yamaguchi, H. Taniguchi, T. Kimura, and H. Takagi: Phys. Rev. B **58** (1998) R1699.

[24] K. Asai, O. Yokokura, N. Nishimori, H. Chou, J. M. Tranquada, G. Shirane, S. Higuchi, Y. Okajima, and K. Kohn: Phys. Rev. B **50** (1994) 3025.

[25] Q. Wei, T. Zhang, X. P. Wang, and Q. F. Fang: Eur. Phys. J. Appl. Phys. **57** (2012) 30401.

[26] Y. Wang and H. J. Fan: J. Appl. Phys. **108** (2010) 053917.

[27] D. Fuchs, C. Pinta, T. Schwarz, P. Schweiss, P. Nagel, S. Schuppler, R. Schneider, M. Merz, G. Roth, and H. v. Löhneysen: Phys. Rev. B **75** (2007) 144402.

[28] P. M. Raccah and J. B. Goodenough: Phys. Rev. **155** (1967) 932.

[29] M. Zhuang, W. Zhang, and N. Ming: Phys. Rev. B **57** (1998) 10705.

[30] Z. Ropka and R. J. Radwanski: Phys. Rev. B **67** (2003) 172401.

[31] M. W. Haverkort, Z. Hu, J. C. Cezar, T. Burnus, H. Hartmann, M. Reuther, C. Zobel, T. Lorenz, A. Tanaka, N. B. Brookes, H. H. Hsieh, H.-J. Lin, C. T. Chen, and L. H. Tjeng: Phys. Rev. Lett. **97** (2006) 176405.

[32] T. Kyômen, Y. Asaka, and M. Itoh: Phys. Rev. B **71** (2005) 024418.

[33] R. H. Potze, G. A. Sawatzky, and M. Abbate: Phys. Rev. B **51** (1995) 11501.

[34] M. A. Korotin, S. Y. Ezhov, I. V. Solovyev, V. I. Anisimov, D. I. Khomskii, and G. A. Sawatzky: Phys. Rev. B **54** (1996) 5309.

[35] G. Jonker and J. V. Santen: Physica **19** (1953) 120.

[36] H. Nakao, T. Murata, D. Bizen, Y. Murakami, K. Ohoyama, K. Yamada, S. Ishiwata, W. Kobayashi, and I. Terasaki: J. Phys. Soc. Jpn. **80** (2011) 023711.

[37] G. Maris, Y. Ren, V. Volotchaev, C. Zobel, T. Lorenz, and T. T. M. Palstra: Phys. Rev. B **67** (2003) 224423.

[38] T. Saitoh, T. Mizokawa, A. Fujimori, M. Abbate, Y. Takeda, and M. Takano: Phys. Rev. B **55** (1997) 4257.

[39] P. Ganguli, P. Guetlich, and E. W. Mueller: Inorg. Chem. **21** (1982) 3429.

[40] R. D. Shannon: Acta Crystallogr. Sect. A **32** (1976) 751.

[41] G. H. Jonker: J. Appl. Phys. **37** (1966) 1424.

[42] J. Li, A. E. Smith, K.-S. Kwong, C. Powell, A. W. Sleight, and M. Subramanian: J. Solid State Chem. **183** (2010) 1388.

[43] K. Knizek, J. Hejtmánek, M. Marysko, Z. Jirak, and J. Bursik: Phys. Rev. B **85** (2012) 134401.

[44] N. Lubinskii, L. Bashkirov, G. Petrov, S. Shevchenko, I. Kandidatova, and I. Sirota: Inorg. Materials **45** (2009) 1026.

[45] S. Okada, A. Sakai, T. Kanno, S. Yotsuhashi, and H. Adachi: J. Appl. Phys. **105** (2009) 083711.

[46] S. Shibasaki, I. Terasaki, E. Nishibori, H. Sawa, J. Lybeck, H. Yamauchi, and M. Karppinen: Phys. Rev. B **83** (2011) 094405.

[47] J. Rodriguez-Carvajal, M. Hennion, F. Moussa, A. H. Moudden, L. Pinsard, and A. Revcolevschi: Phys. Rev. B **57** (1998) R3189.

[48] F. Izumi and K. Momma: Solid State Phenom. **130** (2007) 15.

[49] R. Oishi, M. Yonemura, Y. Nishimaki, S. Torii, A. Hoshikawa, T. Ishigaki, T. Morishima, K. Mori, and T. Kamiyama: Nucl. Instrum. Methods A **600** (2009) 94.

[50] R. Oishi-Tomiyasu, M. Yonemura, and T. Morishima: J. Appl. Crystallogr. **45** (2012) 299.

[51] R. B. Macquart, M. D. Smith, and H.-C. zur Loye: Cryst. Growth Des. **6** (2006) 1361.

[52] J. C. Burley, J. F. Mitchell, and S. Short: Phys. Rev. B **69** (2004) 054401.

[53] D. V. Sheptyakov, V. Y. Pomjakushin, O. A. Drozhzhin, S. Y. Istomin, E. V. Antipov, I. A. Bobrikov, and A. M. Balagurov: Phys. Rev. B **80** (2009) 024409.

[54] R. Caciuffo, J. Mira, J. Rivas, M. A. Senaris-Rodriguez, P. G. Radaelli, F. Carsughi, D. Fiorani, and J. B.Goodenough: Europhys. Lett. **45** (1999) 399.

[55] J. Fujioka, Y. Yamasaki, H. Nakao, R. Kumai, Y. Murakami, M. Nakamura, M. Kawasaki, and Y. Tokura: Phys. Rev. Lett. **111** (2013) 027206.

[56] S. DeGennaro and E. Borchi: Phys. Rev. Lett. **30** (1973) 377.

[57] K. Knizek, Z. Jirak, J. Hejtmánek, M. Veverka, M. Marysko, G. Maris, and T. T.M. Palstra: Eur. Phys. J. B **47** (2005) 213.

[58] S. Yamaguchi, Y. Okimoto, and Y. Tokura: Phys. Rev. B **54** (1996) R11022.

Published Work

- Journal articles

  [1] S. Asai, N. Furuta, Y. Yasui, and I. Terasaki:
  "Weak Ferromagnetism in $LaCo_{1-x}Rh_xO_3$: Anomalous Magnetism Emerging between Two Nonmagnetic End Phases"
  J. Phys. Soc. Jpn. **80** (2011) 104705.

  [2] S. Asai, N. Furuta, R. Okazaki, Y. Yasui, and I. Terasaki:
  "Ga^{3+} substitution effects in the weak ferromagnetic oxide $LaCo_{0.8}Rh_{0.2}O_3$"
  Phys. Rev. B **86** (2012) 014421.

  [3] S. Asai, R. Okazaki, I. Terasaki, Y. Yasui, W. Kobayashi, A. Nakao, K. Kobayashi, R. Kumai, H. Nakao,Y. Murakami, N. Igawa, A. Hoshikawa, T. Ishigaki, O. Parkkima, M. Karppinen, and H. Yamauchi:
  "Spin State of Co^{3+} in $LaCo_{1-x}Rh_xO_3$ Investigated by Structural Phenomena"
  J. Phys. Soc. Jpn. **82** (2013) 114606.

- Proceedings

  [1] S. Asai, R. Okazaki, I. Terasaki, Y. Yasui, N. Igawa, and K. Kakurai:
  "Weak Ferromagnetic Ordering Disordered by Rh^{3+} Ions for $LaCo_{0.8}Rh_{0.2}O_3$"
  JPS Conference Proceedings (in press).

International Conference

[1] S. Asai, N. Furuta, R. Okazaki, Y. Yasui, and I. Terasaki:
" The Anomalous Magnetism of $LaCo_{1-x}Rh_xO_3$ Emerging between Two Non-magnetic End Phases "
CNRS - JSPS Joint Seminar, Nagoya, November 2011.

[2] S. Asai, N. Furuta, R. Okazaki, Y. Yasui, and I. Terasaki: " The Weak Ferromagnetism of $LaCo_{1-x}Rh_xO_3$ Emerging between Two Non-magnetic End Phases "1st Asia-Oceania Conference on Neutron Scattering, Tsukuba, November 2011.

[3] S. Asai, R. Okazaki, Y. Yasui, and I. Terasaki: " Spin state of $LaCoO_3$ investigated from non-magnetic-ion substitution effect of Co sites "The 19th International Conference on Magnetism, Busan, July 2012.

[4] S. Asai, R. Okazaki, Y. Yasui, I. Terasaki, O. Parkkima, H. Yamauchi, and M. Karppinen,: “ Non-magnetic-ion substitution effect of Co sites on spin state of $LaCoO_3$ ”, IGER Annual meeting 2012, Nagoya, January, 2013.

[5] S. Asai, R. Okazaki, I. Terasaki, Y. Yasui, N. Igawa, and K. Kakurai: “ Weak ferromagnetism of $LaCo_{1-x}Rh_xO_3$ driven by controlling the spin state of Co^{3+} ions ”The International Conference on Strongly Correlated Electron Systems 2013, Tokyo, August, 2013.

Acknowledgments

I would like to express my great appreciation to many people helping this research. I first would like to appreciate Professor Ichiro Terasaki for his great advice and supports. His encouragement and guidances help me a lot through this research. I learn many thing about this research from his clever attitude and great perspective for the material science. I would like to thank Professor Hiroki Taniguchi for fruitful advices. I would like to acknowledge Professor Ryuji Okazaki for fruitful discussion on the experimental results and analyses. I would like to thank Professor Yukio Yasui for kind guidances and advice. He has helped and encouraged me a lot for developing the research since I was an undergraduate student. I would like to acknowledge Professor Masatoshi Sato for teaching fundamental attitudes to scientific research.

I would like to express my appreciation to Dr. Takaaki Sudayama for his measurements of x-ray absorption spectra. I would like to thank Dr. Kensuke Kobayashi, Professor Reiji Kumai, Professor Hironori Nakao, and Professor Murakami Yoichi for collaboration in Photon Factory, KEK. I also would like to acknowledge Professor Hironori Nakao for fruitful discussion on my research, in particular on my analysis about the structural properties. I would like to thank Dr. Naoki Igawa and Prof. Kazuhisa Kakurai for collaboration in the neutron scattering measurements at JRR-3. I wish to acknowledge Professor Akinori Hoshikawa and Professor Toru Ishigaki for the assistance in the experiments at iMATERIA, J-PARC. I would like to acknowledge Ms. Outi Parkkima, Professor Maarit Karppinen, and Professor Hisao Yamauchi for helping my three-month stay in Aalto university, Finland and discussion on the experimental results of the thermogravimetric analysis.

I wish to express my gratitude to all the members in the laboratory of Condensed-Matter Physics of Functional Materials for providing the good environments for my research. I would like to thank the staffs of Low Temperature Laboratory for providing the liquid helium and nitrogen. I would like to acknowledge the financial support provided by the Research Fellowship of the Japan Society for Promotion of Science for Young Scientists and the Program for Leading Graduate Schools, Japan Sciety for the Promotion of Science.

Finally, I would like to acknowledge my parents and my brothers for helping me in many ways.